J. Fractal Geom. (Online first)
DOI 10.4171/JFG/129

Published by EMS Press

Geometry and Laplacian on discrete magic carpets

Chunyin Siu and Robert S. Strichartz

Abstract. We study several variants of the classical Sierpinski carpet (SC) fractal. The main examples we call infinite magic carpets (IMC), obtained by taking an infinite blowup of a discrete graph approximation to SC and identifying edges using torus, Klein bottle or projective plane type identifications. We use both theoretical and experimental methods. We prove estimates for the size of metric balls that are close to optimal. We obtain numerical approximations to the spectrum of the graph Laplacian on IMC and to solutions of the associated differential equations: Laplace equation, heat equation and wave equation. We present evidence that the random walk on IMC is transient, and that the full spectral resolution of the Laplacian on IMC involves only continuous spectrum. This paper is a contribution to a general program of eliminating unwanted boundaries in the theory of analysis on fractals.

1. Introduction

The Sierpinski carpet (*SC*) is a classical self-similar fractal generated by an iterated function system of eight contractive similarities in the plane with contraction ratio $1/3$. Figure 1 shows the first three iterations of the approximation to *SC* obtained from the unit square by applying the contractions. Two constructions of a Brownian

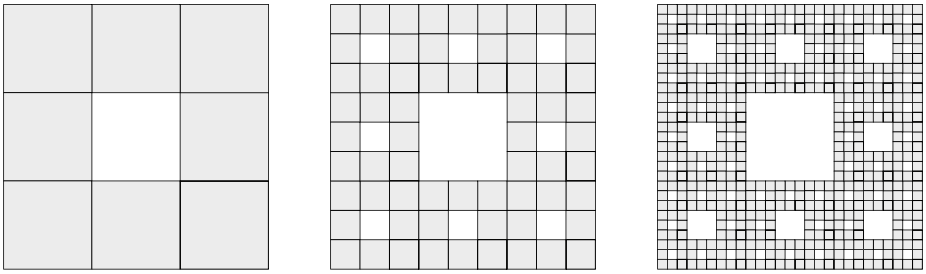

Figure 1. Approximations to *SC*.

2020 Mathematics Subject Classification. 28A80.
Keywords. Fractal, Sierpinski carpet, magic carpets, metric balls, random walk, Laplacian, heat kernel, wave propagator, harmonic functions, Weyl ratio.

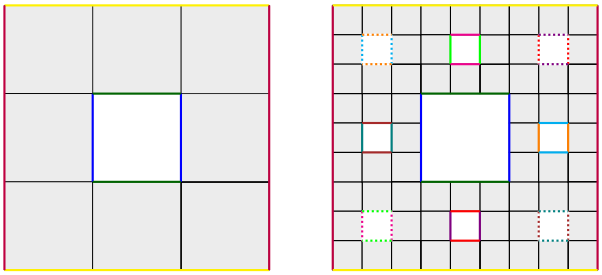

Figure 2. Approximations to *MC*.

motion on *SC* were given by Barlow and Bass [3] and Kusuoka and Zhou [22], and these give rise to a symmetric, self-similar energy (Dirichlet form) and Laplacian. Only recently, in [7] has it been shown that there is, up to a constant multiple, a unique symmetric self-similar Laplacian on *SC*, so the two constructions are equivalent, and also certain passages to subsequences in the constructions are unnecessary. Although the Brownian motion approach yields sub-Gaussian heat kernel estimates, it does not yield detailed information about the eigenvalues and eigenfunctions of the Laplacian (with appropriate boundary conditions). Nevertheless, several experimental approaches have yielded good numerical approximations to the spectrum [9].

One rather vexing question concerns the nature of the analytic boundary of *SC*. (Note that there is no meaningful notion of topological boundary, since *SC* has no interior.) This is usually taken to be the boundary of the square containing *SC*. But a glance at Figure 1 shows that there are infinitely many line segments in *SC* that are locally isometric to portions of this boundary, so the standard choice appears somewhat arbitrary and capricious. In an attempt to get rid of the boundary altogether, a related fractal called the Magic carpet (*MC*) was introduced in [11] and further studied in [25] where potential boundary line segments are identified. Thus the opposite sides of the original square are identified with the same orientation to produce a torus. At stage m of the approximation, 8^{m-1} vacant squares are cut into the previous approximation, and again the opposite sides are identified with the same orientation. This yields a set of 8^m squares (called m-cells) of side length $1/3^m$, and each square has exactly four neighboring squares on the top, bottom, left, and right. We call this cell graph MC_m. See Figure 2 for an illustration of the $m = 1$ and $m = 2$ approximations. Of course, these approximations do not embed in the plane. They should be thought of as surfaces that are flat except for singular points at the corners of identified edges.

In this paper we will denote the above magic carpet by *MCT* to indicate that we have made torus-type identifications of edges. We will also consider *MCK* and *MCP*, where we make Klein bottle or projective plane identifications, as shown in Figure 3.

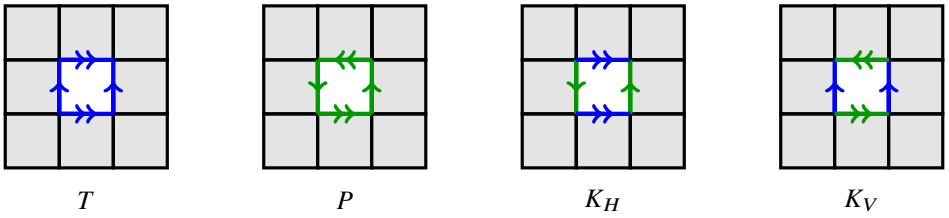

Figure 3. Identification types.

(Note that we could make horizontal or vertical Klein bottle identifications, denoted K_H and K_V, but in this uniform case the two fractals are isometric.) Later, in Section 9, we will consider still other fractals of homogeneous type, where we make one of the four identification types—T, P, K_H, or K_V—on each level.

We will also consider infinite graphs obtained by blowing up the approximations. In other words, take the level-m approximation to MC and regard each m-cell as the vertex of a graph MC_m, and then take the appropriate limit as $m \to \infty$ to obtain the infinite magic carpet graph IMC. More precisely, we write $\widetilde{MC}_m$ to be the cell graph of MC_m without identifying the boundary of the outer square. Then we have embeddings

$$\widetilde{MC}_1 \subseteq \widetilde{MC}_2 \subseteq \cdots$$

and IMC is simply the union. Note that there are many different embedding choices (eight on each level) so IMC is not unique. In the generic case where there is no boundary, it turns out not to matter for what we do here. In the future there may be questions that have different answers depending on these choices. Note that IMC is an infinite 4-regular graph.

We begin by investigating the geometry of the graph IMC. For each fixed vertex, x, let $B(x, r)$ denote the ball of radius r in the geodesic graph metric. What is the cardinality $\#B(x, r)$ as $r \to \infty$? In Section 2 we prove that $\#B(x, r) = O(r^3)$. More precisely, for $IMCT$ and $IMCK$ we have upper and lower bounds of a constant times r^3. For $IMCP$ we obtain the same type of upper bound, but our best lower bound is $c(r/\log r)^3$. We also undertake some numerical experiments that suggest $\lim_{r\to\infty} \#B(x, r)/r^3$ exists for torus and Klein bottle identifications. If this is true for one x, then the same limit holds for all x.

In Section 3 we examine random walks on IMC. The main question is to decide whether these are recurrent or transient. Random walks on fractals (or associated graphs) have been studied extensively [2, 4–6, 8, 10, 19]. We gather numerical data of random walks on the IMC on two fronts: (i) we compute the percentage of walks that return to the starting point as the length of the walk varies, and (ii) we compute the effective resistance from a fixed point to the boundary of a large square (which

should tend to infinity if the walk is recurrent and remain bounded if the walk is transient, cf. [12, 34]). Neither test is decisive, but we present the data.

In Section 4 we study the spectrum of the graph Laplacian, $-\Delta u(x) = u(x) - \frac{1}{4}\sum_{y\sim x} u(y)$, on *IMC*. Here the main question is whether the spectrum is pure-point, continuous, or a mixture of the two. In order to explore the possibility of square-summable eigenfunctions (point spectrum), we numerically solve the Dirichlet problem $-\Delta u = \lambda u$ inside $\widetilde{MC}_m$ for large m with $u \equiv 0$ on the boundary. If u were a square-summable eigenfunction, then eventually it would be very close to zero on a large neighborhood of the boundary of $\widetilde{MC}_m$, and so it would be very close to one of the Dirichlet eigenfunctions, and this Dirichlet eigenfunction would vanish rapidly as you approach the boundary. We do not see any such Dirichlet eigenfunctions, so this provides strong numerical evidence that the spectrum is continuous.

This also tells us that the Dirichlet spectrum is unrelated to the spectrum of *IMC*. Nevertheless, as we will see later, the data is not completely useless, as it allows us to study the heat kernel.

In Section 5 we study the heat kernel on *IMC* by approximating it by the Dirichlet heat kernel on $\widetilde{MC}_m$, given by

$$H_t^{(m)}(x,y) = \sum_i e^{-\lambda_i t} u_i(x) u_i(y),$$

where $\{u_i\}$ is an orthonormal basis of Dirichlet eigenfunctions on $\widetilde{MC}_m$ with eigenvalues λ_i (all of these depend on m, of course, but we prefer not to burden the notation to make this explicit). Since the heat kernel is highly localized, if x and y are not too close to the boundary, the choice of Dirichlet boundary conditions should have only a negligible effect on the heat kernel. The two fundamental questions here concern the on-diagonal behavior and the off-diagonal behavior. For $x = y$, we ask if there is some power law behavior

$$H_t(x,x) = O(t^{-\beta}) \qquad \text{as} \qquad t \to \infty \tag{1.1}$$

for some β. Surprisingly, our data suggest that instead of (1.1), it is more likely that

$$H_t(x,x) = O(t^{-\beta(x)}) \qquad \text{as} \qquad t \to \infty$$

where $\beta(x)$ depends on x. We present data to support this. The $\beta(x)$ values for x far from the boundary satisfy $\beta(x) > 1$. For the off-diagonal behavior, we fix y and t, and examine the decay of $H_t(x,y)$ as x moves away from y. We present two types of data: (i) the graph of $H_t(x,y)$ as a function of x as x varies along a line segment in *IMC* containing y, and (ii) a scatter plot of the values of $H_t(x,y)$, where x varies over all points of distance r to y, with r varying. Because these values of the heat kernel are close to zero, the graphs of $\log H_t(x,y)$ reveal more information.

In Section 6 we study the wave propagator

$$W_t^{(m)}(x,y) = \sum_i \frac{\sin\sqrt{\lambda_i}t}{\sqrt{\lambda_i}} u_i(x)u_i(y) \tag{1.2}$$

that provides the solution

$$u(x,t) = \sum_y \left(W_t^{(m)}(x,y)\, g(y) + \frac{d\,W_t^{(m)}}{dt}\Big|_{(x,y)} f(y) \right)$$

to the wave equation

$$\frac{\partial^2 u}{\partial t^2} = \Delta^{(m)} u$$

(where $\Delta^{(m)}$ denotes the Laplacian on $\widetilde{MC}_m$) with initial conditions

$$u(x,0) = f(x) \qquad \text{and} \qquad \frac{\partial u}{\partial t}(x,0) = g(x).$$

The wave propagator is relatively localized for small t, so that our approximations give interesting information about wave propagation on the *IMC* graph.

In Section 7 we study harmonic functions and the analog of the Poisson kernel on $\widetilde{MC}_m$ obtained by setting boundary values $P(x,y) = \delta_{xy}$ for y a fixed point, x a variable point on the boundary, and $\Delta_x^{(m)} P(x,y) = 0$ for x in the interior. The Poisson kernel decays as x moves away from y, as seen in the graphs and scatter plots, but not as rapidly as the heat kernel. An interesting question that we have not been able to deal with is whether or not there is an analog of Liouville's Theorem: are bounded harmonic functions necessarily constant?

In Section 8 we return to the finite fractal setting. By considering MC_m as consisting of cells of size $1/3^m$ we obtain approximations to the original magic carpet *MCT*. We also do the same for the other identification types to obtain *MCP* and *MCK*. We find the convergence of eigenvalues as we vary m with respect to a Laplacian renormalization factor R that is slightly larger than 6 (it varies slightly with the identification type), and we can observe the refinement of eigenfunctions as m increases by using an averaging process to pass from functions on level $m+1$ to functions on level m. We also see miniaturization of eigenfunctions that produce periodic eigenfunctions that are translates on copies of V_m of a certain size. These may also be interpreted as periodic eigenfunctions on *IMC*, analogous to the functions $\cos \lambda k$ (for rational λ) on the integers.

We then compute the eigenvalue counting function,

$$N(t) = \#\{\lambda_i : \lambda_i \le t\},$$

and the Weyl ratio,

$$W(t) = \frac{N(t)}{t^\alpha} \qquad \text{for} \qquad \alpha = \frac{\log 8}{\log R}.$$

(Here, $1/8$ is the renormalization factor for the standard measure on *MC*.) Note that $\alpha > 1$. This is quite different than for *SC* [9]. The three different identification types

yield qualitatively different Weyl ratio graphs. We do not see any periodicity in the log-log plots of $W(t)$.

In Section 9 we continue in the finite fractal setting, but we allow the identification type to change from level to level. We call these *homogeneous* magic carpets. Now there are actually four possibilities since the two Klein bottle identifications—horizontal, K_H, and vertical, K_V—are not always interchangeable if used on different levels. Thus we write T, P, K_H, K_V, T for $m = 4$ identifications, where the first T means to identify the outer boundary by T, the sides of the single large vacant square by P, the next eight largest vacant squares by K_H, and so on. We note that the final identification on the smallest level does not influence the spectrum, but of course, it would lead to different fractals if we continued in the limit. On level 4, this leads to $256 = 4^4$ possible spectra, some of which are equivalent. Here we look at a representative sample, including all sixteen involving just T and P. All cases are included in the website [15]. The question we would like to answer is the following: is there a qualitative procedure to use the Weyl ratio to deduce the particular identifications chosen? An idea proposed in [13] called spectral segmentation is that different segments of the spectrum relate to the identification types at different levels. While we are unable to support this hypothesis in full generality, we are able to see the signature of the first k choices in the beginning segments of increasing length for $k = 1, 2, 3$.

In Section 10 we discuss the experimental evidence that the spectral resolution of the Laplacian on *IMC* is purely continuous.

For the reader's convenience, the figures used after Section 2 are collected in Appendix A.

Many of the ideas discussed in this paper are still conjectural, but we present a lot of data in figures and tables to support these conjectures experimentally. The website [15] contains much more data. For the general theory of Laplacian on fractals the reader may consult the books [1], [21] and [30].

2. Cardinality

The distance between cells x and y, $d(x, y)$, in the identified magic carpet blowup, *IMC*, is defined to be the length of the shortest path through cells from x to y. Recall that we denote the ball of radius r around a cell x by

$$B(x, r) = \{y: y \text{ is a cell of } IMC \text{ with } d(x, y) < r\},$$

whose cardinality will be denoted $\#B(x, r)$. The level-m approximation to *IMC*, including the inner identifications, is denoted by V_m. An identification that is done at level $m + 1$ will be called an *m-stitch*. With this notation, V_{m+1} contains eight copies of V_m and one m-stitch.

2.1. The lower bound for torus and Klein identifications

In this section we derive the r^3 lower bound for torus and Klein identifications. In each case, the argument is the same. Projective identifications are deferred to Section 2.2.

Consider first torus identifications. The left image of Figure 4 shows a path of length 10 across V_2. To find a path across V_3, we may duplicate the path across V_2 and add six steps through the five red cells. We obtain the path of length 26 in the image on the right. To find a path across any higher V_{m+1}, we may repeat this process: duplicate the path across V_m and add six steps through cells positioned as the red cells are. Letting r_m be the length of this path across V_m, these lengths satisfy

$$r_{m+1} = 2r_m + 6 \qquad \text{with} \qquad r_2 = 10,$$

which has solution

$$r_m = 2^{m+2} - 6. \tag{2.1}$$

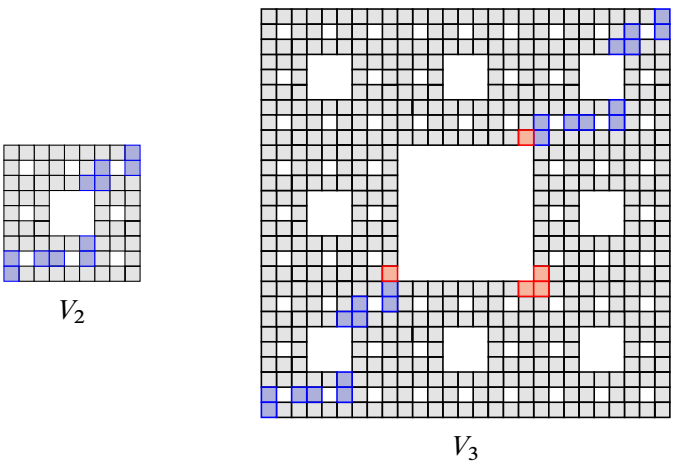

Figure 4. Paths of lengths $r_2 = 10$ and $r_3 = 26$ with torus identifications.

Lemma 2.1. *Given r_m steps, a path from a corner cell of V_m can reach any other cell in V_m.*

Proof. First, consider torus identifications. We induct on m with base case V_2. We check this case by hand on the left of Figure 5; indeed, all cells may be reached within r_2 steps.

Assume that, from a corner in V_m, any cell in V_m can be reached within r_m steps. Consider a corner cell x of V_{m+1}. Starting at x, within r_m steps we can reach a cell at the corner of the m-stitch of V_{m+1}. From here, we can reach a corner of each of the

7	7	6	5	4	3	2	1	0
6		5	4		3	2		1
7	7	6	5	5	4	3	2	2
7	6	5				4	3	3
7		6				5		4
8	7	6				5	4	5
9	8	7	6	6	5	6	5	6
9		8	7		6	7		7
10	9	9	8	7	7	7	6	7

7	7	6	5	4	3	2	1	0
6		5	4		3	2		1
7	7	6	5	5	4	3	2	2
8	7	6				4	3	3
7		6				5		4
7	6	5				5	4	5
8	7	6	6	6	5	6	5	6
8		7	7		6	7		7
9	8	8	8	7	7	7	6	7

Figure 5. A number in a cell indicates, among all paths entirely within V_2, the length of a shortest path to the top right cell. On the left, we use torus identifications, and on the right, we use Klein horizontal.

other seven copies of V_m within six steps. (These six steps are the steps through some of the red cells in Figure 4, or through their mirror image after a diagonal reflection.) Applying the inductive hypothesis again, we can reach any cell in each of these other copies of V_m within an additional r_m steps. Adding these up, we can go from x to any other cell in V_{m+1} within $2r_m + 6 = r_{m+1}$ steps.

For Klein bottle identifications, each cell of V_2 can be reached from the corner cell within nine steps. Again, this can be verified by hand, as in Figure 5. Finally, in V_{m+1}, any two copies of V_m can be joined by a path across the m-stitch. Such a path can be found with at most six steps, like the red path in the torus example of Figure 4. ∎

Lemma 2.2. *For every cell x, we have $\#B(x, 2r_m + 1) \geq 8^m$.*

Proof. By Lemma 2.1, we can travel from x to a corner of the copy of V_m containing x within r_m steps, and from there we can travel to any other cell in the same copy of V_m with an additional r_m steps. Hence $B(x, 2r_m + 1) \supseteq V_m$, and so

$$\#B(x, 2r_m + 1) \geq 8^m.$$ ∎

2.2. A lower bound for projective identifications

Let us now consider the case of projective identifications. We obtain a looser bound. The issue is that with projective identifications, an m-stitch does not quickly connect all copies of V_m, and so we must use longer paths.

Consider a sequence R_m satisfying

$$R_0 = 0 \quad \text{and} \quad R_{m+1} = \max\{2R_m + 3, \quad 2R_m + 2^m + 1\}.$$

Lemma 2.3. *Given R_m steps, a path from any cell of V_m can reach any other cell in V_m.*

Proof. It suffices to prove the induction step, as the base case $m = 0$ is trivial. Suppose the path goes from cell x to cell y. First suppose x is in the top middle copy of V_m, as highlighted in Figure 6 (a). Inductively from x, it takes at most R_m steps to reach a corner cell by the m-stitch, e.g., a blue or green cell in Figure 6 (b). From there, it can reach any other copy of V_m within three steps, and then it takes at most another R_m steps to reach y.

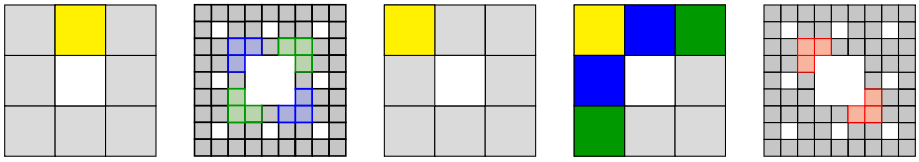

Figure 6. Illustration for the proof of Lemma 2.3.

Next, suppose x is in the corner copy, as in Figure 6 (c). If y is not in one of the green copies of V_m in Figure 6 (d), a path from x can reach one of the red cells of Figure 6 (e) using R_m or fewer steps. Thus x and y are at most $2R_m + 3$ steps apart.

If y is in a green copy, the path can reach y by traversing one of the blue copies shown in Figure 6 (d); this can be achieved in $2^m - 1$ steps straight across the blue V_m, as in Figure 7. In addition to the (upper bound of) $2R_m$ steps needed to get from x to the outer boundary of a blue copy and to get from the outer boundary of a blue copy to y, it takes one step to enter the blue copy and one step to leave the blue copy. Hence the path has at most $2R_m + 2^m - 1 + 2$ steps, and the result follows. ∎

Lemma 2.4. *When $m \geq m_0 \geq 2$,*

$$R_m \leq \frac{1}{2}\left(m \cdot 2^m\right) + \left(\frac{R_{m_0} + 1}{2^{m_0}} - \frac{m_0}{2}\right)\left(2^m\right) - 1.$$

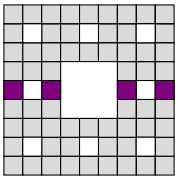

Figure 7. A path across V_m of length $2^m - 1$.

Proof. Note that when $m \geq 2$,

$$R_m = 2R_{m-1} + 2^{m-1} + 1.$$

Therefore, when $k = 1$,

$$R_m \leq 2^k R_{m-k} + k \cdot 2^{m-1} + 2^k - 1.$$

We prove that this inequality holds for $1 \leq k \leq m - m_0 - 1$ by induction on k as follows:

$$\begin{aligned} R_m &\leq 2^k R_{m-k} + k \cdot 2^{m-1} + 2^k - 1 \\ &\leq 2^k (2R_{m-k-1} + 2^{m-k-1} + 1) + k \cdot 2^{m-1} + 2^k - 1 \\ &\leq 2^{k+1} R_{m-(k+1)} + (k+1) \cdot 2^{m-1} + 2^{k+1} + 1. \end{aligned}$$

Then, for $k = m - m_0$,

$$\begin{aligned} R_m &\leq 2^{m-m_0} R_{m_0} + (m - m_0) \cdot 2^{m-1} + 2^{m-m_0} - 1 \\ &= \frac{1}{2}(m \cdot 2^m) + \Big(\frac{R_{m_0} + 1}{2^{m_0}} - \frac{m_0}{2}\Big)(2^m) - 1. \end{aligned}$$

■

Lemma 2.5. *For every cell x and m large enough, $\#B(x, m \cdot 2^m) \geq 8^m$.*

Proof. We have $\#B(x, R_m) \geq 8^m$ by Lemma 2.3, and $R_m \leq m \cdot 2^m$ for large enough m by Lemma 2.4. ■

2.3. The upper bound

We present the upper bound in the case of any of our three identifications: torus, Klein, or projective. The main idea is if a path has fewer than $2^m - 1$ steps, then it cannot cross a copy of V_m (Lemma 2.7), hence is trapped in certain neighboring copies of V_m (Corollary 2.16). Crossing is made rigorous using m-edges, which we now define.

If ℓ is a line segment in *IMC* along which two distinct copies of V_m intersect after identifications, then call ℓ an *m-edge*. Denote by $E_{V,W}$ the m-edge along which the copies V and W of V_m intersect. We say that a cell is on an m-edge if one of its edges lies on the m-edge.

An m-edge is *vertical* (or *horizontal*, respectively) if it is vertical (horizontal) in the *IMC* before identification (more precisely, if its preimage before identification is a union of vertical edges). Two copies of V_m are *horizontal neighbors* (or *vertical neighbors*, respectively) if they intersect along a vertical (horizontal) m-edge.

Lemma 2.6. *Within a copy of V_m, there are 2^m columns of cells that do not hit any vertical m'-stitch for $m' \leq m - 1$.*

Proof. Starting with $m = 0$, for which there is indeed $1 = 2^0$ column, we induct on m. Consider V_{m+1}, which contains eight copies of V_m. Notice that the three copies of V_m on the left of the central m-stitch—and hence the 2^m columns of cells they contain—stack one on top of the next (Figure 8). Since there is an m-stitch, the same does not happen in the center, but it does happen on the right side; so, there are $2 \cdot 2^m = 2^{m+1}$ columns in V_{m+1} that do not hit any m-stitch, as desired. ∎

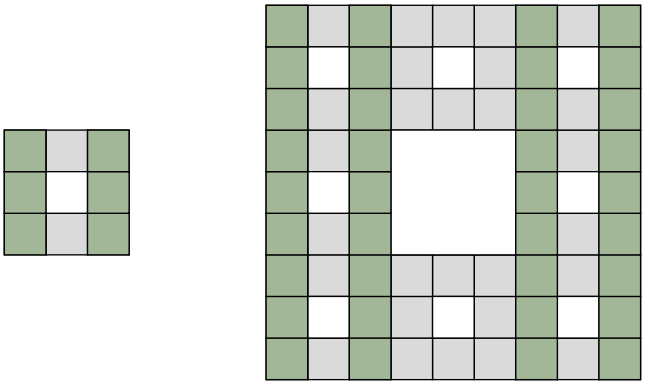

Figure 8. The two columns in V_1 and the four columns in V_2.

Lemma 2.7. *Consider a path inside a copy of V_m with at most $2^m - 1$ steps. If the path begins along an m-edge of the copy of V_m, then it cannot leave along the opposite m-edge.*

Proof. Without loss of generality, assume a path goes between the left and right sides. From Lemma 2.6 we obtain 2^m columns of cells in V_m that do not intersect any m'-stitches for $m' \leq m - 1$. Since the path is constrained to V_m, it cannot use any M-stitches for $M \geq m$, so it must traverse each of these 2^m columns. This requires $2^m - 1$ steps, and so the path cannot leave the copy of V_m through the opposite m-edge. ∎

Lemma 2.7 prevents paths that are too short from crossing a copy of V_m.

Example 2.8. In Figure 9, a path cannot connect the blue m-edge to the green m-edge without leaving the copy of V_m shown, unless it has $2^m - 1$ or more steps.

Our last result was restricted to paths inside a particular copy of V_m; we must now remove this restriction. Our goal is to show first that a short path remains within a few consecutive copies of V_m, and second that these copies all share a vertex. Because our path must whirl around this common vertex, we shall call it the center. To make this precise, let us first introduce m-stacks, m-sequences, and m-segments-of-two.

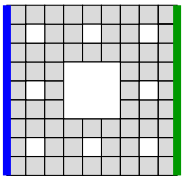

Figure 9. Opposite m-edges in a copy of V_m.

An *m-stack* is a finite sequence of copies of V_m such that consecutive copies are all horizontal neighbors or all vertical neighbors. A cell is in an m-stack if it is in a copy of V_m in the stack. Observe that every m-stack—as a cell graph—is isomorphic to a sequence of copies of V_m with the bottom edge of each copy glued to the top edge to the previous one with edge orientations preserved (Figure 10). Hence, every m-stack has a rectangular outer boundary. A *side* of an m-stack is a side of this outer boundary. A cell is on a side if it intersects with the side.

Lemma 2.7 essentially provides the following result, as well:

Corollary 2.9. *If a path is contained in an m-stack and has cells on two opposite sides, then its length is at least $2^m - 1$.*

Consider a finite path γ as a sequence of cells: $c_0, c_1, c_2, \ldots, c_n$. From γ we form a sequence of copies of V_m as follows:

(1) For each c_i, find the copy $V_m^{c_i}$ of V_m containing c_i, and form a new sequence $V_m^{c_1}, \ldots, V_m^{c_n}$.

(2) While consecutive elements in this new sequence are equal, delete all but one of them.

What remains after these deletions, we call the *m-sequence* of γ. In other words, the first copy in the m-sequence is the copy of V_m that contains the starting cell, the second term is the copy containing the first cell c_i that is not in the first copy, the third copy is that containing the first cell after c_i that is not in the second copy, and so on.

For an m-sequence, we define an *m-segment-of-two* as a tuple (i, V, W) such that V is the ith copy of V_m in the m-sequence, W is the $(i+1)$st copy, and neither V nor W is the $(i-1)$st copy (if it exists). The m-segments-of-two from a particular m-sequence are clearly ordered by their first entries. Note that if (i, V, W) is an m-segment-of-two, then V and W form an m-stack.

The jth copy of V_m in the m-sequence of a path is in an m-segment-of-two (i, V, W) if and only if all copies inclusively between the ith and the jth copies are either V or W. A cell c is in an m-segment-of-two if and only if the copy of

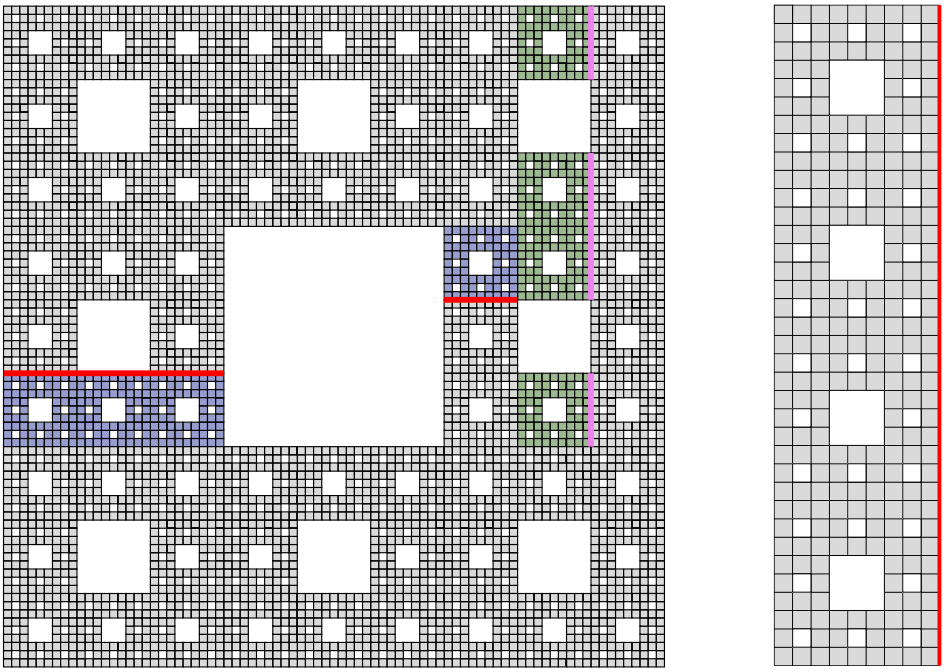

Figure 10. Two different 2-stacks (one blue, one green, and containing four copies of V_2 each) in a copy of V_4 with Klein identifications. Both 2-stacks are equivalent to the rectangular 2-stack shown on the right.

V_m containing c is in the m-segment-of-two. Observe that all copies of V_m in an m-segment-of-two (i, V, W) are either V or W.

Example 2.10. Fix $m = 1$ and consider the blue path through V_2 shown in Figure 11. The figure marks four copies of V_1, namely, U, V, W and X. The m-sequence of the path is U, V, U, W, X. There are three m-segments-of-two: the first, $(1, U, V)$, contains the first three terms of the m-sequence; the next, $(3, U, W)$, contains the third and the fourth terms; and the last, $(4, W, X)$, contains the final two terms.

A path $(c_0, c_1, \dots)$ is said to *enter* an m-segment-of-two (i, V, W) through an m-edge if there are consecutive cells c_n, c_{n+1} so that (1) both are on the m-edge, and (2) only c_{n+1} is within (i, V, W). The notion of a path *exiting* is analogous, with c_n in (i, V, W) instead. The m-edge along which the path enters (i, V, W) is denoted by $\mathrm{Ent}(i)$, and the m-edge along which it exits is denoted $\mathrm{Exit}(i)$.

Example 2.11 (Continuing Example 2.10). Figure 11 distinguishes the following m-edges:

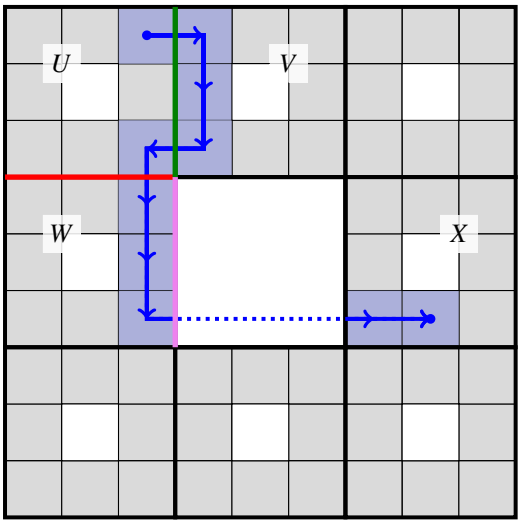

Figure 11. A sample path in V_2 (proceeding downwards, roughly, and then to the right).

m-segment-of-two	Enter	Color	Exit	Color
$(1, U, V)$	–	–	Exit(1)	red
$(3, U, W)$	Ent(3)	green	Exit(3)	pink
$(4, W, X)$	Ent(4)	red	–	–

Recall here that if V and W are copies of V_m, then $E_{V,W}$ is the m-edge along which V and W intersect.

Lemma 2.12. *Let (i, V, W) be an m-segment-of-two associated to a path of length at most 2^m.*

(1) *Each of* Ent(i) *and* Exit(i) *(assuming it exists) is distinct from $E_{V,W}$, although, it intersects $E_{V,W}$.*

(2) *If* Ent(i) *and* Exit(i) *both exist (i.e., the path comes from and goes to other copies of V_m), then they are on the same side of the m-stack formed by V and W, and hence,* Ent(i), Exit(i) *and $E_{V,W}$ all intersect at one vertex.*

Proof. For the first claim, it suffices to consider Ent(i); the case for Exit(i) is similar. By the definitions of m-segments-of-two and entering, Ent(i), if it exists, cannot be $E_{V,W}$. Since the path must go from V to W, it has cells on $E_{V,W}$; furthermore, since the path has at most 2^m steps, and one step is required to enter the m-segment-of-two, Corollary 2.9 prevents it from entering through an m-edge parallel to $E_{V,W}$. The first claim follows, for the remaining edges of the m-stack formed by V and W all intersect $E_{V,W}$.

For the second statement, suppose $\mathrm{Ent}(i)$ and $\mathrm{Exit}(i)$ are on different sides of the m-segment-of-two. Counting the steps needed to enter and exit, Lemma 2.9 implies the path has more than 2^m cells, a contradiction. Since $\mathrm{Ent}(i)$ and $\mathrm{Exit}(i)$ are on the same side, they both intersect the same endpoint of $E_{V,W}$, which, since $\mathrm{Ent}(i)$ and $E_{V,W}$ are distinct, is the only point where $\mathrm{Ent}(i)$ and $E_{V,W}$ intersect. ∎

Consider a path with at most 2^m steps and at least two m-segments-of-two. Since the path has at least two m-segments-of-two, for each m-segment-of-two (i, V, W), at least one of $\mathrm{Ent}(i)$ and $\mathrm{Exit}(i)$ exists. Define the *center* of the m-segment-of-two (i, V, W) to be the vertex where $E_{V,W}$, $\mathrm{Ent}(i)$ and $\mathrm{Exit}(i)$ (or those that exist) intersect. Notice that the center will always be a corner vertex of V and W. The lemma above ensures the center is well-defined.

Example 2.13. Figure 12 shows a green path of length 3 and a blue path of length 4. Forming the 0-sequence associated to the green path, we see its center is marked by the pink dot. Due to the torus identifications taken in this picture, the center of the blue path is represented by four points, the red dots.

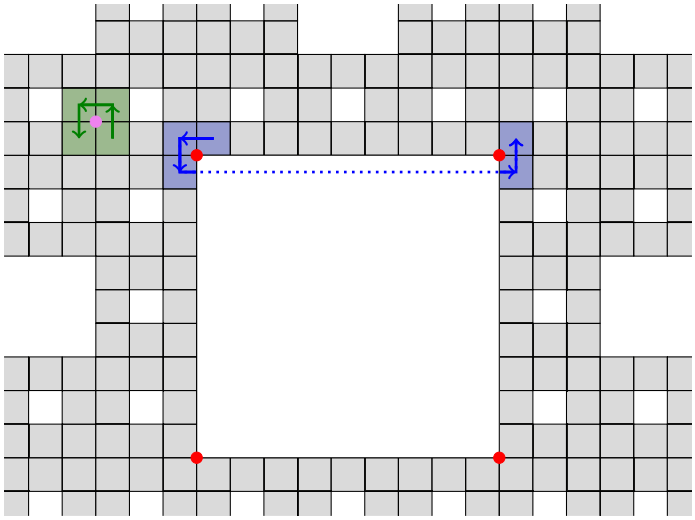

Figure 12. The centers of two paths.

Lemma 2.14. *Consider a path with at most 2^m steps and at least two m-segments-of-two. The centers of the m-segments-of-two are the same.*

Proof. Let us limit our focus to consecutive m-segments-of-two: say, (i, V, W) and (j, X, Y), where $i < j$, $X \in \{V, W\}$, and $Y \notin \{V, W\}$. We show that the centers are

the same, and induction completes the argument. Note that the path enters (j, X, Y) through $E_{V,W}$ and exits (i, V, W) at $E_{X,Y}$. The center of (i, V, W), therefore, is where $\text{Exit}(i) = E_{X,Y}$ intersects $E_{V,W}$, and the center of (j, X, Y) is where $\text{Ent}(j) = E_{V,W}$ intersects $E_{X,Y}$. Hence, the intersection of $E_{V,W}$ and $E_{X,Y}$ marks both centers. ∎

Lemma 2.15. *For a path of length at most 2^m, let U be the first copy of V_m in the associated m-sequence. There exists a corner vertex x of U shared by every copy of V_m in the m-sequence.*

Proof. First, if U is the only copy of V_m in the m-sequence, the result holds. Second, when there is only one m-segment-of-two, $(1, V, W)$, we may choose any vertex shared by the two relevant copies V and W.

If the path has at least two m-segments-of-two, then the centers of all m-segments-of-two are the same by Lemma 2.14. In particular, the centers are the same as that of the first m-segment-of-two. Since the center of the first m-segment-of-two is a vertex of U, the result follows from the fact that every m-cell touches the center of an m-segment-of-two. ∎

The proof shows the center often suffices for this common vertex. The only time it does not is for paths with one m-segment-of-two, when the center is undefined. The existence of this vertex then gives:

Corollary 2.16. *Consider $z \in IMC$, and denote by V_z the copy of V_m containing z. Define $\mathcal{V}$ to be the set of all copies of $V_m \subset IMC$ that share a corner vertex with V_z. Any path from z with length at most $2^m - 1$ remains within $\bigcup_{V\in\mathcal{V}} V$; that is,*

$$B(z, 2^m) \subseteq \bigcup_{V\in\mathcal{V}} V.$$

Lemma 2.17. *With the notation of Corollary 2.16, $\#\mathcal{V} \leq 45$.*

Proof. Consider a corner x of V_z. If x is a corner of a stitch, then V_z touches at most 11 other copies of V_m at x (Figure 13). Otherwise, it touches only 3 other copies of V_m at x. Counting at most 11 copies for each of the four outer vertices of V_z, along with V_z itself, we have

$$\#\mathcal{V} \leq 4 \cdot 11 + 1 = 45.$$ ∎

Remark 2.18. The count of 45 in Lemma 2.17 is sufficient for our purposes, but it can be improved to 21. Doing so improves the constant 2880 appearing within the proof of Theorem 2.19. Briefly, given a copy V of V_m, we must count all 8 copies of V_m in the same copy of V_{m+1} as vertex-sharing neighbors. Next, find the smallest copy of V_M containing V but not with V along an M-edge (so V is not on the "boundary" of

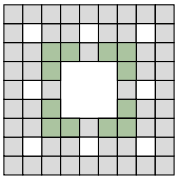

Figure 13. A copy of V_m can share a vertex with eleven other copies through the stitch.

this copy of V_M). Then V is on an $(M-1)$-edge inside this copy of V_M. If V touches an $(M-1)$-stitch at exactly one vertex, a corner, as in the case shown in Figure 14, then it has 13 additional neighbors: 11 near corners of the stitch and 2 not touching the $(M-1)$-stitch, colored green and red in the figure. If V touches the $(M-1)$-stitch along its side or not at all, then it has fewer neighbors.

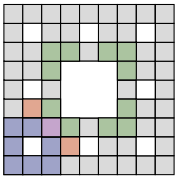

Figure 14. The main case needed to improve the count, where V (purple) touches the stitch at one corner.

2.4. Full bound

Here we combine the upper and lower bounds above, first for torus and Klein identifications and then for projective identifications.

Theorem 2.19. *Let $x \in IMC$ with either torus or Klein identifications. Then we have $\#B(x,r) \sim r^3$; that is, there are constants c and C so that when r is sufficiently large,*

$$c r^3 \le \#B(x,r) \le C r^3.$$

Proof. For any r, we can find m so that

$$2^{m-1} \le r+1 \le 2^m.$$

With the notation of Section 2.1, specifically (2.1), we can write

$$2r_{m-4}+1 = 2^{m-1} - 11 \le r \le 2^m.$$

Lemma 2.2 then gives us the lower bound

$$\#B(x,r) \ge \#B(x, 2r_{m-4}+1) \ge 8^{m-4}.$$

Further, Corollary 2.16 and Lemma 2.17 yield the upper bound

$$\#B(x,r) \le \#B(x,2^m) \le \#\mathcal{V} \cdot 8^m \le 45 \cdot 8^m.$$

Additionally, if r is sufficiently large, then $2^{m-2} \le r \le 2^m$, in which case

$$\frac{1}{8^m} \le \frac{1}{r^3} \le \frac{1}{8^{m-2}}.$$

Apply the lower and upper bounds to obtain

$$\frac{8^{m-4}}{8^m} \le \frac{\#B(x,2r_{m-4}+1)}{r^3} \le \frac{\#B(x,r)}{r^3} \le \frac{\#B(x,2^m)}{r^3} \le \frac{45 \cdot 8^m}{8^{m-2}}.$$

Hence

$$\frac{1}{4096} r^3 \le \#B(x,r) \le 2880 r^3.$$

■

Remark 2.20. The upper bound holds on the infinite magic carpet with any identifications. The lower bound holds even when torus and Klein styles are mixed together, so long as there are no projective identifications. Hence $\#B(x,r) \sim r^3$ for any mixture of torus and Klein identifications.

Now we turn to projective identifications.

Theorem 2.21. *With projective identifications, for large enough r,*

$$c\left(\frac{r}{\log r}\right)^3 \le \#B(x,r) \le C r^3.$$

Proof. The upper bound holds as mentioned above, so it suffices to consider the lower bound. Choose $m \cdot 2^m < r \le (m+1) \cdot 2^{m+1}$; then

$$\log m + m \log 2 < \log r,$$

in which case $m \log 2 < \log r$. Then, for sufficiently large r,

$$m + 1 < 2 \cdot \frac{\log r}{\log 2}.$$

Using this to substitute for $\log r$ along with Lemma 2.5, we find

$$\begin{aligned}
\frac{\#B(x,r)}{(r/\log r)^3} &\ge \frac{8^m \cdot (\log r)^3}{((m+1) \cdot 2^{m+1})^3} \\
&\ge \frac{8^m \cdot (m+1)^3 (\log 2/2)^3}{((m+1) \cdot 2^{m+1})^3} \\
&= \frac{8^{m-1} \cdot (\log 2)^3}{8^{m+1}} \\
&= \frac{(\log 2)^3}{64}.
\end{aligned}$$

■

2.5. The cardinality ratio

Let us briefly consider the cardinality ratio $\#B(x,r)/r^3$. We show how this ratio behaves with each identification type around two sample points in Figure 15. The plots suggest this ratio may converge, although we do not have proof of this. Of course, this conjecture is less certain for projective identifications, where even the $\sim r^3$ growth rate is unknown. We can say, however, that if this ratio converges, then it will converge consistently over all cells.

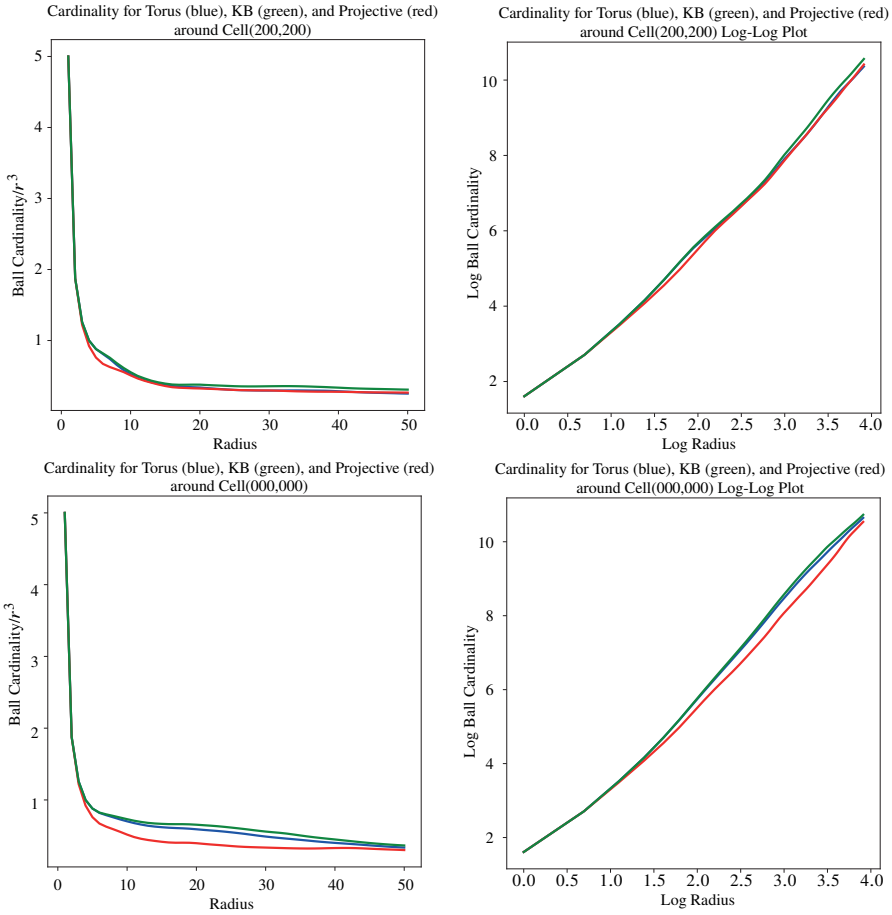

Figure 15. The ball cardinality ratio $\#B(x,r)/r^3$ around two sample points (left), each beside a corresponding $\log \#B(x,r)$-to-$\log r$ plot (right).

Proposition 2.22. *Fix any identification type and any two cells x and y. If*

$$\lim_{r\to\infty} \frac{\#B(x,r)}{r^3} = c, \qquad \textit{then also} \qquad \lim_{r\to\infty} \frac{\#B(y,r)}{r^3} = c.$$

Proof. For large r, the triangle inequality provides $\#B(x, r - d(x, y)) \leq \#B(y, r) \leq \#B(x, r + d(x, y))$, from which

$$\lim_{r\to\infty} \frac{\#B(x, r - d(x, y))}{r^3} \leq \lim_{r\to\infty} \frac{\#B(y, r)}{r^3} \leq \lim_{r\to\infty} \frac{\#B(x, r + d(x, y))}{r^3}.$$

Our assumption $\#B(x, r)/r^3 \to c$ may be used to compute these bounds. For the lower bound,

$$\lim_{r\to\infty} \frac{\#B(x, r - d(x, y))}{r^3} = \lim_{r\to\infty} \frac{\#B(x, r - d(x, y))}{(r - d(x, y))^3} \cdot \frac{(r - d(x, y))^3}{r^3} = c,$$

and similarly for the upper bound. ∎

3. Random walks

In this section, we present data from our computer simulation concerning random walks on the *IMC* and the effective resistance from a fixed point to the boundaries of large squares.

The random walk simulation was carried out on the *IMC* obtained by applying the repeated application of the inverses of the contractions that fix two opposite vertices. The starting points were chosen to be the cell whose lower left hand corner is $(0, 0)$ before identification. Only the simple symmetric random walk was considered, i.e., the random walker has equal probability, $1/4$, of moving upwards, downwards, to the left, and to the right. A trial terminates either when the random walker has returned to the starting point, in which case the walk is said to be empirically recurrent, or when the walker has walked a prescribed number of steps, the maximum length. If a trial is not empirically recurrent, it is said to be empirically transient. The length of a trial is the number of steps the walker has walked when the trial terminates.

We note that in each simulation, roughly $2/3$ of all trials are empirically recurrent. Even though the computations are not conclusive, they suggest the walk is transient. The results of the simulations are summarized in Table 1.

Concerning the lengths of empirically recurrent trials, a power law was observed for each of *IMCT*, *IMCK* and *IMCP*. We are thankful for an anonymous reviewer's suggestion which helped us find this behavior. To be precise, let

$$p_n = P(\text{walk length} = n),$$

and suppose for some $C > 0$ and $\alpha > 1$ that

$$p_n \sim C n^{-\alpha}.$$

In estimating α, there is the difficulty that for many n no simulated walk returned in exactly n steps; indeed, there are many more possible lengths than there are simulations. For this reason, we first group the empirically recurrent walk lengths n into

	identification	no. of trials	max. length	number (percentage) of empirically recurrent trials
	torus	2 000	500 000	1 348 (67.4%)
	torus	500	1 000 000	331 (66.1%)
†	torus	2 000	10 000 000	1 390 (69.5%)
	torus	200	100 000 000	137 (68.5%)
	Klein bottle	1 000	500 000	667 (66.7%)
	projective plane	1 000	500 000	683 (68.3%)

Table 1. Results of random walk simulations on infinite magic carpets.

logarithmic-scale bins $e^{j-\frac{1}{2}} \le n < e^{j+\frac{1}{2}}$. This can give an estimate for q_j, the probability that a returning walk has length in the bin $e^{j-\frac{1}{2}} \le n < e^{j+\frac{1}{2}}$. This ought to be

$$q_j = \sum_{e^{j-\frac{1}{2}} \le n < e^{j+\frac{1}{2}}} p_n \approx \frac{C}{1-\alpha} e^{j(1-\alpha)} \left(e^{\frac{1-\alpha}{2}} - e^{-\frac{1-\alpha}{2}} \right),$$

here approximating the sum over n by an integral. Hence,

$$\log q_j \approx (1-\alpha)\, j + \log\left[\frac{C}{1-\alpha} \left(e^{\frac{1-\alpha}{2}} - e^{-\frac{1-\alpha}{2}} \right) \right],$$

and so the logs of these relative frequencies q_j are expected to look linear with slope $1-\alpha$ when plotted against j. Estimating q_j with the empirically recurrent random walk simulations and plotting these estimates for $\log q_j$ against j yields Figures 16 and 17, which are now discussed.

The trials on *IMCT* with maximum length 10 000 000 (row † in Table 1) appear in Figure 16. The apparent linear trend is consistent with a power law. Linear regression on the data points—excluding the leftmost (likely not yet convergent) and rightmost (likely too few walks to be reliable)—gives a linear fit with correlation coefficient -0.965, indicating a strong correlation. The fitted slope is -0.211, and hence $\alpha \approx 1.211$.

The corresponding plots for *IMCK* and *IMCP*, based on data on the last two rows of Table 1, are shown in Figure 17. The correlation coefficients are -0.921 and -0.943; the fitted slopes are -0.269 and -0.257, and hence $\alpha \approx 1.269$ and $\alpha \approx 1.257$ for *IMCK* and *IMCP*.

Walk length data can be found on the website [15].

As for the effective resistance, the resistance from each cell to the outermost square boundary of the mth approximation of the *IMC* with torus identification was computed for $m = 2, 3, 4$. High computation cost rendered direct computation impractical for larger m. Instead, a number of cells in the 5th approximation are randomly

selected to compute their resistances. The resistance of a cell to the boundary is computed by solving the harmonic equation with the value at the cell fixed to be one and those at the boundary cells fixed to be zero.

If the random walk is transient, the resistances should remain bounded, and if recurrent, the resistances should diverge as in the case $\mathbb{Z}^2$ (cf. [12]). The results are summarized in Table 2 and Figure 18. Which occurs is unclear from these resistances, since we only have $m = 2, 3, 4$. (The resistances of squares in $\mathbb{Z}^2$ are included in Figure 19 for comparison.)

m	max. resistance on mth approximation
2	0.385
3	0.521
4	0.629

Table 2. Maximum Resistances of Cells on the mth Approximation of the *IMC*.

As shown in Figure 18, the resistances follow a hill-shaped trend as the distance from the boundary varies. Unlike the case for $\mathbb{Z}^2$, in Figure 19, the maximum resistance for each distance does not increase monotonically as the cell moves away from the boundary, but peaks at around $2/3$ of the maximum distance. Since only data for $m = 2, 3, 4$ are gathered, it is difficult to infer the behavior of the resistances for larger m, and hence the nature of the random walk on the *IMC*.

4. Spectrum of the graph Laplacian on *IMC*

For each of the identification types, we would like to speculate on the structure of the spectrum of the Laplacian on *IMC* by doing calculations on $\widetilde{MC}_m$ for $m \leq 4$. Suppose, for example, that there were a square summable eigenfunction $\phi(x)$. Then it would have to vanish as $x \to \infty$. In particular, on $\widetilde{MC}_m$ for large enough m it would have to be very close to zero on a neighborhood of the boundary squares. It would also have to be close to a Dirichlet eigenfunction (one that vanishes on the boundary). So we compute all of the Dirichlet eigenfunctions and examine them to see if they are close to zero in a neighborhood of the boundary. We show some samples from the first 150 in Figure 20. Many more (the first 150 for each identification type) can be found on the website [15]. None of the first 150 appears to have this decay property. We take this as evidence that the spectrum of the Laplacian on *IMC* is entirely continuous. Of course, we were limited by our computational resources to $m \leq 4$, so it is conceivable, although unlikely, that a discrete spectrum only makes an appearance at larger

values of m. In Section 8 we will construct a countable family of bounded periodic eigenfunctions on *IMC*. In Section 10 we conjecture that these provide the spectral resolution of the Laplacian on *IMC* with a purely continuous spectrum.

Our Dirichlet eigenfunctions and corresponding tables of values have no relationship to the *IMC* spectrum, but we will use them in Section 5 to approximate the heat kernel on *IMC*.

5. The heat kernel on *IMC*

As mentioned in the Introduction, we have computed the heat kernel on MC_m for $m = 4$. For points x, y far from the boundary and moderate t, we expect this to be a good approximation to the heat kernel on *IMC*. It is, of course, interesting to understand the behavior of the heat kernel on *IMC* for large values of t, but we are limited by our computational resources to get a handle on this question. Complete data is available on the website [15].

The first question we consider is the on-diagonal behavior, $H_t(x, x)$. From other fractal models we were led to expect a power law behavior [1], but instead found that power varies with the point. In Figure 21 we show the graph of $H_t(x, x)$ as a function of t for a small sample of points x on a log-log scale. Here and elsewhere we focus mainly on the cells x bordering the largest removed square, since these are relatively far from the outer boundary. We take the approximate slope of the portion of the graph that appears close to linear to estimate $-\beta(x)$. In Table 3 we list these values for the aforementioned cells. In Figure 22 we show histograms of these values. This supplies evidence that *IMC* is very inhomogeneous. It is not clear whether or not the gaps in the histograms would persist if we were able to extend the computation to higher values of m.

Next, we consider the off-diagonal behavior of the heat kernel. We fix y and t, and examine the graph of $x \mapsto H_t(x, y)$. In Figure 23 we show some samples. As expected, we see a rapid decay as x moves away from y. To see this more clearly, we look at the restriction of x to a line segment passing through y in Figure 24. We have also graphed scatter plots of the values of $H_t(x, y)$ for all x of distance k to y as k varies (again, log-log plots), as shown in Figure 25. From this we obtain conjectural bounds

$$c_1 e^{-c_2 d(x,y)^{\gamma}} \le H_t(x, y) \le c_1' e^{-c_2' d(x,y)^{\gamma'}},$$

where c_1, c_2, c_1', c_2' depend on y and t, and

$$a \le \gamma \le b \qquad \text{and} \qquad a' \le \gamma' \le b'.$$

For estimates of γ and γ', plots of $\log(-\log(H_t(x, y)))$ against distance $d(x, y)$ suggest linear bounds with slopes $\gamma < 1.348$ and $\gamma' > 0.7038$.

Slope according to identification type							
	Cell	Torus	Projective	Klein		Cell	Klein
0	(1000, 0222)	−1.301726	−1.263855	−1.304539	28	(2000, 1000)	−1.304547
1	(1001, 0222)	−1.253730	−1.239121	−1.257284	29	(2000, 1001)	−1.256358
2	(1002, 0222)	−1.221663	−1.216606	−1.225863	30	(2000, 1002)	−1.223405
3	(1010, 0222)	−1.202318	−1.202270	−1.206413	31	(2000, 1010)	−1.203137
4	(1011, 0222)	−1.198272	−1.199859	−1.201669	32	(2000, 1011)	−1.198634
5	(1012, 0222)	−1.183683	−1.187111	−1.187614	33	(2000, 1012)	−1.184506
6	(1020, 0222)	−1.174705	−1.179356	−1.178552	34	(2000, 1020)	−1.176441
7	(1021, 0222)	−1.171706	−1.176650	−1.174911	35	(2000, 1021)	−1.174205
8	(1022, 0222)	−1.164308	−1.168956	−1.166984	36	(2000, 1022)	−1.166854
9	(1100, 0222)	−1.163814	−1.168638	−1.166578	37	(2000, 1100)	−1.166354
10	(1101, 0222)	−1.170175	−1.175674	−1.173650	38	(2000, 1101)	−1.172659
11	(1102, 0222)	−1.171464	−1.177031	−1.175646	39	(2000, 1102)	−1.173191
12	(1110, 0222)	−1.177146	−1.182105	−1.181406	40	(2000, 1110)	−1.177974
13	(1111, 0222)	−1.186926	−1.190956	−1.190607	41	(2000, 1111)	−1.187285
14	(1112, 0222)	−1.177146	−1.182105	−1.181406	42	(2000, 1112)	−1.177974
15	(1120, 0222)	−1.171464	−1.177031	−1.175646	43	(2000, 1120)	−1.173191
16	(1121, 0222)	−1.170175	−1.175674	−1.173650	44	(2000, 1121)	−1.172659
17	(1122, 0222)	−1.163814	−1.168638	−1.166578	45	(2000, 1122)	−1.166354
18	(1200, 0222)	−1.164308	−1.168956	−1.166984	46	(2000, 1200)	−1.166854
19	(1201, 0222)	−1.171706	−1.176650	−1.174911	47	(2000, 1201)	−1.174205
20	(1202, 0222)	−1.174705	−1.179356	−1.178552	48	(2000, 1202)	−1.176441
21	(1210, 0222)	−1.183683	−1.187111	−1.187614	49	(2000, 1210)	−1.184506
22	(1211, 0222)	−1.198272	−1.199859	−1.201669	50	(2000, 1211)	−1.198634
23	(1212, 0222)	−1.202318	−1.202270	−1.206413	51	(2000, 1212)	−1.203137
24	(1220, 0222)	−1.221663	−1.216606	−1.225863	52	(2000, 1220)	−1.223405
25	(1221, 0222)	−1.253730	−1.239121	−1.257284	53	(2000, 1221)	−1.256358
26	(1222, 0222)	−1.301726	−1.263855	−1.304539	54	(2000, 1222)	−1.304547
27	(2000, 0222)	−1.301722	−1.263856	−1.304540	55	(2000, 2000)	−1.304540

Table 3. Approximate slopes of the log-log Dirichlet heat kernel, calculated along the region $-1 \leq \log t \leq 3$. (Note that the heat kernel is nonlinear.) The cells listed are those along the edge of the central, removed square. There are twice as many for Klein horizontal identifications because of the asymmetry in that case.

6. The wave propagator on *IMC*

In Figures 26–27 we show the graphs of the wave propagator (1.2) as a function of x for $m = 4$ and three different choices of y with $t = 1, 2, 3, 4$. These are all shown with torus identifications. Note that we do not expect a finite propagation speed, since we are working on a graph, but we do expect most of the significant support to be centered at y and to increase with t (but some other fractals—non-discrete ones—do have non-finite propagation speed, see [23]). Comparing $t = 1$ with $t = 2$ and $t = 2$ with $t = 4$, we see a qualitative spreading of the size of the significant support, although we do not see how to make this into a quantitative statement.

The maximum value seems to occur near $x = y$ but not always at $x = y$, and the propagator appears to be bounded. This is in contrast to the propagator in $\mathbb{R}^2$ that has a singularity at $|x - y| = t$.

In Figures 28–29 we show scatter plots of wave propagator values for cells near x.

7. Harmonic functions

Harmonic functions on *IMC* are characterized by the property that the value at any cell is equal to the average value on the four neighboring cells. We expect that the space of harmonic functions is infinite-dimensional, so in particular, on any of the approximations $\widetilde{MC}_m$, there are nonzero harmonic functions that are close to zero. Thus we cannot learn very much about the full space of harmonic functions on *IMC* by studying harmonic functions on $\widetilde{MC}_m$. Nevertheless, it is interesting to study the analog of the Poisson kernel on $\widetilde{MC}_m$.

For this purpose we define the boundary of $\widetilde{MC}_m$ to be the $4\,(3^m - 1)$ cells along the boundary of the square containing $\widetilde{MC}_m$, and everything else forms the interior. We impose the harmonic condition only on interior cells, and prescribe values on the boundary cells. The Poisson kernel $P(x, y)$ is the function that provides the interior values in terms of the boundary values

$$h(x) = \sum_{y \in \partial \widetilde{MC}_m} P(x, y) h(y).$$

It follows from general principles that such a function exists uniquely and is nonnegative. In fact, $x \mapsto P(x, y)$ is the unique harmonic function satisfying $P(x, z) = \delta_{xz}$ for z in the boundary. So $P(y, y) = 1$ and $P(x, y)$ is expected to decay as x moves away from y, but not as rapidly as the heat kernel.

In Figure 30 we show graphs of $x \mapsto P(x, y)$ for a sampling of points y, all with torus identifications. We also show scatter plots of the values of $P(x, y)$ as x varies over cells of distance k to y.

8. Spectrum of the Laplacian on magic carpet fractals

Let MC_m denote the level-m approximation with the outer boundary identified in the same manner as the inner boundaries (so we have three versions: MCT_m, MCK_m, and MCP_m). So MC_m has 8^m cells; we assign to each of them measure $1/8^m$, and we take the side lengths to be $1/3^m$, so each MC_{m+1} is a refinement of MC_m in the appropriate sense. Then MC_m should be a good proxy of MC for large m. The Laplacian on MC_m is given by

$$-\Delta^{(m)} f(x) = \sum_{y \underset{m}{\sim} x} (f(x) - f(y)) .$$

It is a symmetric operator with 8^m eigenfunctions with eigenvalues in $[0, 8]$ (by the circle theorem of Geršgorin). We would like to claim the existence of a limiting operator

$$-\Delta f = \lim_{m \to \infty} R^m \Delta^{(m)} f$$

on MC for the appropriate renormalization factor R. Then the spectrum of $-\Delta$ would be the limit of the spectrum of $\Delta^{(m)}$ multiplied by R^m. In fact, there is no published proof of the existence of this limit, but numerical data in this paper and in previous works ([11], [25] in the torus identification case) leaves little doubt that the limit exists.

By computing the spectra for $m = 2, 3, 4$ and taking ratios we can estimate the renormalization factor R. This data is shown in Tables 4–6 for the beginning of the spectrum, and the remainder can be found on the website [15].

We notice that the ratios decrease as you move farther up the spectrum, and we believe that computational error degrades the results as the eigenvalues increase, so we take the average of the first ten ratios λ_3/λ_4 from each table to estimate

$$R_T \approx 6.441049, \qquad R_K \approx 6.373221, \qquad \text{and} \qquad R_P \approx 6.326518.$$

These are close but not equal. Note that some of the eigenvalues for the torus and projective identifications have multiplicity two. This is easily explained by the fact that MCT and MCP have a dihedral D_4 group of symmetries, and D_4 has a two-dimensional irreducible representation. The symmetry group of MCK is $\mathbb{Z}_2 \times \mathbb{Z}_2$, which is abelian, so it only has one-dimensional irreducible representations. As can be seen in Tables 4 and 5, the location in the spectrum of the multiplicity two eigenvalues agrees from one level m to the next only in the bottom portion of the spectrum, so the use of ratios is only meaningful below these points.

In Figure 31 we show the graphs of the eigenvalue counting functions, and in Figure 32 the Weyl ratio (log-log).

We observe that the different identification types produce qualitatively different Weyl ratios, but for large values of t they are very similar because of the fact that the

	Torus glued identifications				
	Eigenvalue λ_2 for $M = 2$	Eigenvalue λ_3 for $M = 3$	Eigenvalue λ_4 for $M = 4$	Ratio λ_2/λ_3	Ratio λ_3/λ_4
0	0.0	0.0	−0.0	–	–
1	0.4410218	0.0718171	0.0110916	6.1408993	6.4749219
2	** 0.690591	** 0.1119098	** 0.0173466	6.1709581	6.4513906
3	** 0.690591	** 0.1119098	** 0.0173466	6.1709581	6.4513906
4	0.7587998	0.1205024	0.0185273	6.2969667	6.5040388
5	1.4269914	0.2334006	0.0359611	6.1139159	6.4903591
6	** 1.482754	** 0.245267	** 0.0379436	6.0454696	6.4639853
7	** 1.482754	** 0.245267	** 0.0379436	6.0454696	6.4639853
8	1.4983881	0.2518546	0.0392556	5.949417	6.415758
9	1.5692227	0.2780838	0.0438667	5.6429846	6.3392857
10	1.8746245	0.3402416	0.053536	5.509687	6.3553786
11	** 1.8836369	** 0.3455927	** 0.0552662	5.4504528	6.2532401
12	** 1.8836369	** 0.3455927	** 0.0552662	5.4504528	6.2532401
13	2.0	** 0.415878	** 0.0649221	4.8091024	6.4058044
14	2.3293357	** 0.415878	** 0.0649221	5.6010068	6.4058044
15	** 2.4155337	0.4189091	0.0658944	5.7662475	6.3572796

Table 4. The beginning eigenvalues with torus glued identifications at levels $m = 2, 3, 4$, and the ratios of these eigenvalues.

	Projective plane glued identifications				
	Eigenvalue λ_2 for $M = 2$	Eigenvalue λ_3 for $M = 3$	Eigenvalue λ_4 for $M = 4$	Ratio λ_2/λ_3	Ratio λ_3/λ_4
0	−0.0	−0.0	−0.0	–	–
1	0.3058223	0.0477565	0.0074541	6.4037878	6.406704
2	0.4410218	0.0729375	0.0115116	6.046572	6.3360045
3	0.7587998	0.1233985	0.0194031	6.1491843	6.3597326
4	** 1.1250751	** 0.1858666	** 0.0292749	6.0531309	6.3490018
5	** 1.1250751	** 0.1858666	** 0.0292749	6.0531309	6.3490018
6	1.3324988	0.2338597	0.0373292	5.6978556	6.2647901
7	1.3652037	0.2388857	0.0380849	5.7148832	6.2724489
8	1.4983881	0.254542	0.0403709	5.8866048	6.3050832
9	1.5692227	0.2898892	0.0466163	5.4131807	6.2186257
10	1.8746245	0.3058223	0.0477565	6.1297834	6.4037878
11	** 2.0	0.3422554	** 0.0541734	5.8435898	6.3177806
12	** 2.0	** 0.343133	** 0.0541734	5.8286443	6.3339803
13	** 2.0371299	** 0.343133	0.0548889	5.9368529	6.2514145
14	** 2.0371299	0.4275677	0.0690194	4.7644621	6.1948905
15	2.1109942	0.430103	0.0697148	4.9081133	6.1694614

Table 5. As in Table 4, but the identifications here are projective.

Klein bottle horizontal glued identifications					
	Eigenvalue λ_2 for $M = 2$	Eigenvalue λ_3 for $M = 3$	Eigenvalue λ_4 for $M = 4$	Ratio λ_2/λ_3	Ratio λ_3/λ_4
0	0.0	0.0	−0.0	–	–
1	0.4410218	0.0723638	0.0112916	6.0945093	6.408612
2	0.690591	0.1119495	0.0173792	6.1687743	6.4415609
3	0.757329	0.121964	0.018978	6.2094458	6.4266102
4	0.7587998	0.123382	0.0193997	6.1500041	6.3599916
5	1.1250751	0.1852829	0.0290511	6.0722031	6.3778205
6	1.482754	0.2465753	0.0384654	6.0133933	6.410307
7	1.4983881	0.2530836	0.0398039	5.920527	6.3582652
8	1.5692227	0.2844123	0.0453381	5.5174219	6.2731406
9	1.8662197	0.3196011	0.0507154	5.8392155	6.3018541
10	1.8746245	0.3415234	0.0535803	5.4890069	6.3740525
11	1.8836369	0.3429855	0.054342	5.491885	6.3116066
12	1.9260699	0.3463405	0.055662	5.5612036	6.2222017
13	2.0	0.356565	0.0576952	5.6090762	6.1801455
14	2.0371299	0.4067644	0.0640321	5.0081327	6.3525108
15	2.3293357	0.4245981	0.0675213	5.4859772	6.2883567

Table 6. As in Table 4, but the identifications here are Klein bottle horizontal.

$m = 4$ approximation loses accuracy. We also observe that the Weyl ratios are not multiplicatively periodic. This will have implications in the next section.

In Figure 33, we show a sampling of graphs of eigenfunctions for $m = 4$. One interesting phenomenon that we observe among levels is a miniaturization of eigenfunctions, as in Figure 34. Thus, every eigenfunction on level $m - 1$ reappears at level m repeated 8 times on each of the smaller subsquares, with the same eigenvalue, and of course, this iterates. This happens for all three identifications. The general procedure is illustrated in Figure 35. We can turn this observation around to attempt to describe bounded periodic eigenfunctions on *IMC*. Take any eigenfunction of $-\Delta^{(m)}$ on MC_m and duplicate it on every copy of MC_m in *IMC*. This produces an exact eigenfunction on *IMC* that is bounded and periodic. We will use these in Section 10 to attempt to describe the spectral resolution on *IMC*.

In order to understand the relationship between the eigenfunctions of $-\Delta^{(m)}$ for different values of m that should be regarded as refinements, we use the following reverse comparison by an averaging method. Start with an eigenfunction u on MC_m, so $-\Delta^{(m)}u = \lambda^{(m)}u$. Now produce a function $\bar{u}$ on MC_{m-1} by assigning to a cell x in MC_{m-1} the average value of u on the eight cells in MC_m that comprise x. Compute $-\Delta^{(m-1)}\bar{u}$ and look for a value $\lambda^{(m-1)}$ that is an eigenvalue of $-\Delta^{(m-1)}$ such that $-\Delta^{(m-1)}\bar{u} \approx \lambda^{(m-1)}\bar{u}$. Then compare $\bar{u}$ to its projection proj $\bar{u}$ on the $\lambda^{(m-1)}$-eigen-

space. We consider u a refinement if proj $\bar{u}$ is close to $\bar{u}$. In many instances, it is, as shown in Figure 36. However, this cannot always be the case, simply because there are many more eigenvalues on level m than on level $m-1$. We do not see evidence of the spectral decimation property as established on the Sierpinski gasket in [14].

9. Homogeneous identifications

Rather than use the same type of identification at all levels in constructing MC_m, we may vary the type from level to level. For example,

$$MC_4(T, P, K_H, K_V, T)$$

means we do torus identifications on the outer boundary, projective identifications on the one large vacant square, horizontal Klein bottle identifications on the eight next largest vacant squares, and so on. At the lowest level of a cell-graph approximation, two cells are neighbors independent of identification type. Unlike higher level gaps, the orientation of edges does not influence the fact that the cells are neighbors. We can observe this clearly on MC_1, with fixed outer identification, where any identification type for the interior, vacant square yields the same cell graph. Hence the final identification type on the smallest vacant squares does not affect the spectrum at this level, but of course, if we think of this as an approximation to a magic carpet fractal, this identification will play a role in the later approximations. The idea for looking at these is inspired by the work of Hambly [16] on Sierpinski-gasket-type fractals, and the followup in [13]. We call these *homogeneous* because we use the same identification type across the board on each level. We could also consider the more general situation where every identification is allowed for each vacant square, as in [17, 18], but we do not expect to see any structure in the spectrum with such choices.

For $m = 4$, there are $4^4 = 256$ choices for identification types, although some interchanges of K_H and K_V will yield the same spectrum. To keep things manageable, we mainly concentrate on torus and projective identifications, which reduces the total number to sixteen. In Figure 38 we show the simultaneous graphs of eight Weyl ratios for all identification types that begin with T (respectively, P). In Figure 39 we show a zoom of these graphs to the beginning interval $[-5, -2]$. In Figures 40–43 we show the simultaneous graphs of four Weyl ratios with the same first two identification types, again with zooms to the interval $[-5, -2]$. In Figures 44–51 we show simultaneous graphs of two Weyl ratios with the same first three identification types, with zooms to the interval $[-5, -2]$.

A general principle called *spectral segmentation* was introduced in [13] to the effect that it is possible to segment the spectrum of a fractal Laplacian so that each segment corresponds to the geometry at a certain scale. For the example studied in

[13], this effect, although only qualitative, was immediately apparent visually. What made the situation so clear was the fact that the Weyl ratios for the underlying Sierpinski gaskets were asymptotically multiplicatively periodic. That is not the case here, as mentioned in Section 8.

What the graphical evidence shown in the figures is supposed to suggest is a weak form of this principle: if two identification sequences agree in the first k places, then the Weyl ratios are qualitatively the same for $\log t \le a_k$, where a_k increases with k.

10. The spectral resolution on *IMC*

We can use the periodic eigenfunctions discussed in Section 8 to attempt to describe the spectral resolution on *IMC* in a spirit similar to [31]. We refer the reader to [29] for details on functional analysis. For each interval $[a,b)$ we need to construct a projection operator $P_{[a,b)}$ on $\ell^2(IMC)$ that is additive, and so that

$$f = \lim_{b\to\infty} P_{[0,b)} f \tag{10.1}$$

and

$$-\Delta f = \int_0^\infty \lambda \, dP_{[0,\lambda)} f. \tag{10.2}$$

These identities should hold for all $f \in \ell^2(IMC)$ but it suffices to verify them for f having compact support.

Let $\{u_k^{(m)}\}$ denote an orthonormal basis of eigenfunctions on $\widetilde{MC}_m$, so

$$-\Delta^{(m)} u_k^{(m)} = \lambda_k^{(m)} u_k^{(m)},$$

and let $\tilde{u}_k^{(m)}$ denote the periodic extension to *IMC* as illustrated in Figure 35. Suppose m is large enough that the support of f is contained in the interior of $\widetilde{MC}_m$. Then

$$\sum_k \langle f, \tilde{u}_k^{(m)} \rangle \tilde{u}_k^{(m)} = f \qquad \text{on } \widetilde{MC}_m, \tag{10.3}$$

where $\langle f, \tilde{u}_k^{(m)} \rangle$ denotes $\sum_{x\in \mathrm{supp}\, f} f(x)\tilde{u}_k^{(m)}(x)$, and

$$\sum_k \langle f, \tilde{u}_k^{(m)} \rangle \lambda_k \tilde{u}_k^{(m)} = -\Delta f \qquad \text{on } \widetilde{MC}_m. \tag{10.4}$$

So we define

$$P_{[a,b)}^{(m)} f = \sum_{\lambda_k^{(m)} \in [a,b)} \langle f, \tilde{u}_k^{(m)} \rangle \tilde{u}_k^{(m)},$$

and we conjecture that the following limit [24, 27] exists:

$$P_{[a,b)} f = \lim_{m\to\infty} P_{[a,b)}^{(m)} f.$$

If so, then (10.1) follows from (10.3), and (10.2) follows from (10.4).

A. Figures

For the reader's convenience, the figures referred to in the text from Section 3 onward are collected in this appendix.

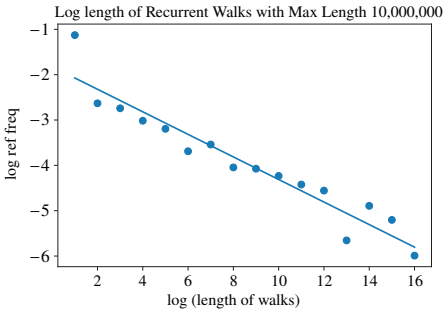

Figure 16. Estimates for the log relative bin frequencies, $\log q_j$, on *IMCT* using data from Table 1 row †. The horizontal axis represents j, the log-scale midpoint of the bin $e^{j-\frac{1}{2}} \le n < e^{j+\frac{1}{2}}$.

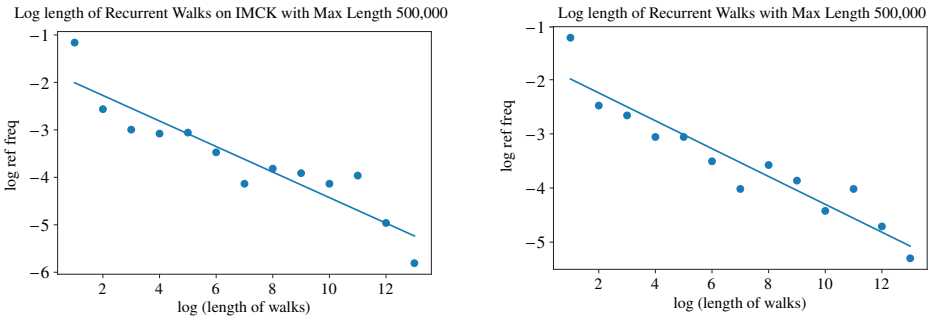

Figure 17. As in Figure 16, here for *IMCK* and *IMCP*.

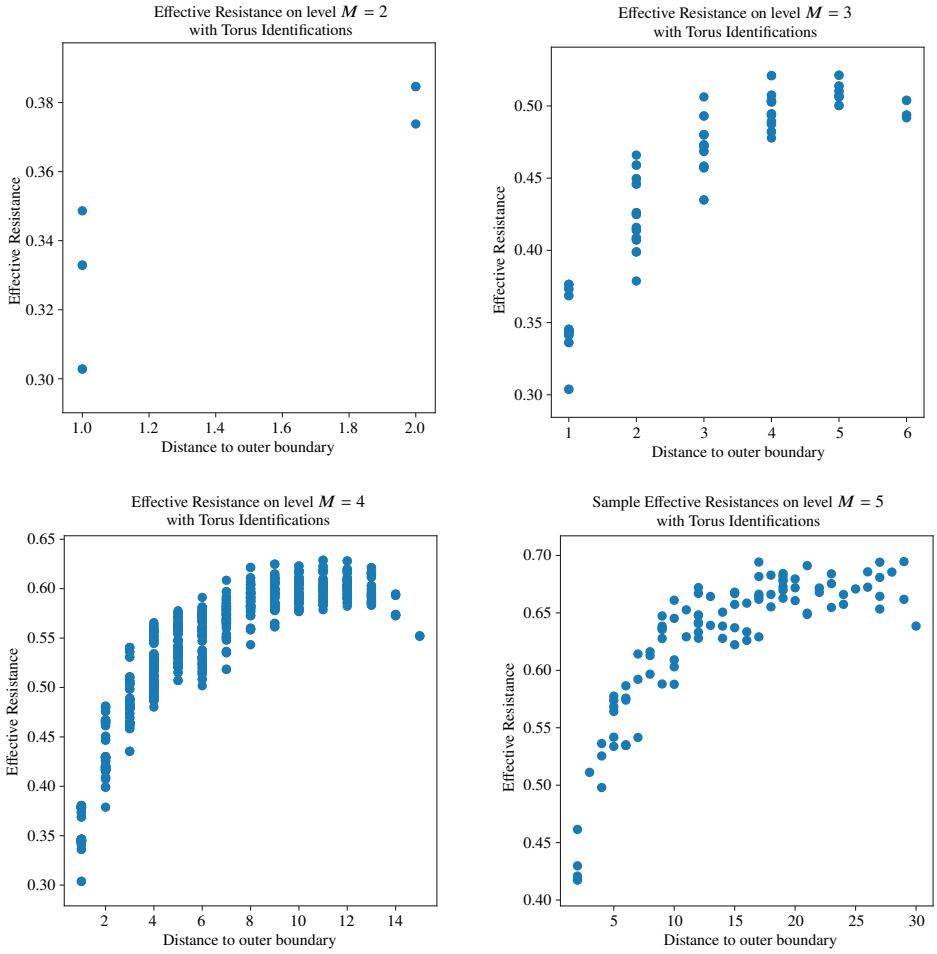

Figure 18. Effective resistances with torus identifications, at levels $M = 2$ (top left), 3 (top right), 4 (bottom left). For level 5 (bottom right), only some sample points are shown.

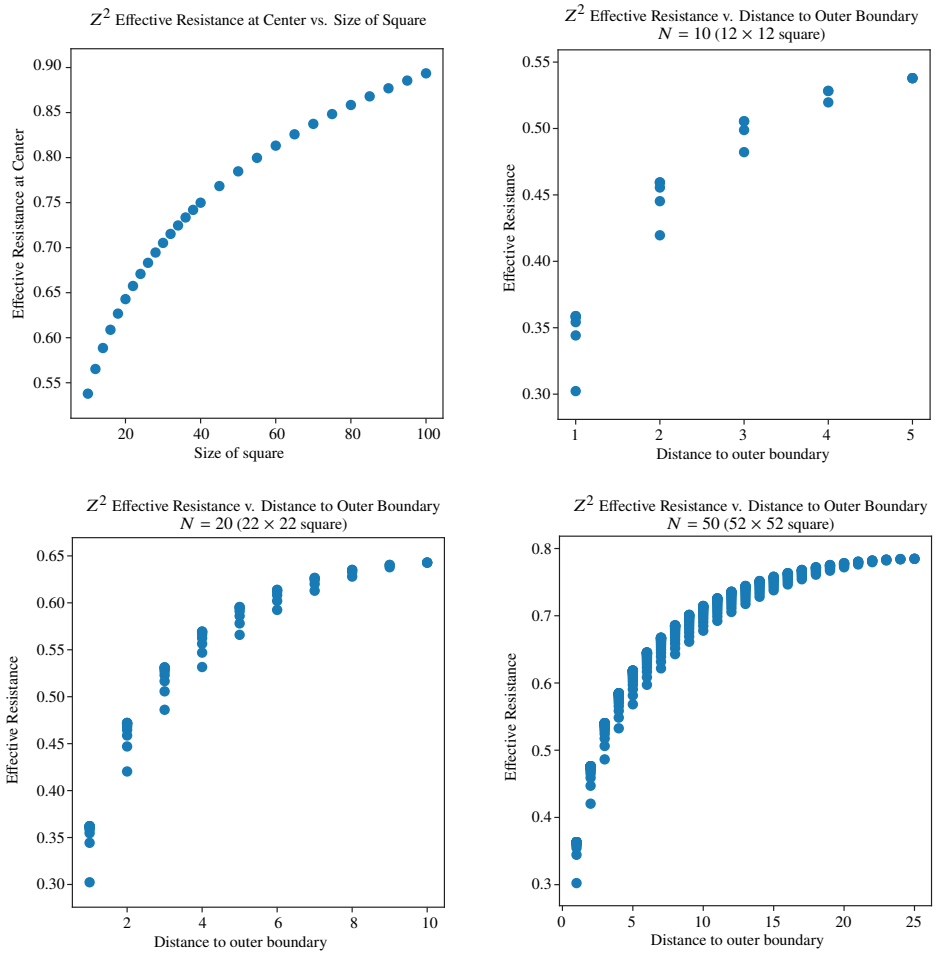

Figure 19. Effective resistances on the $\mathbb{Z}^2$ lattice.

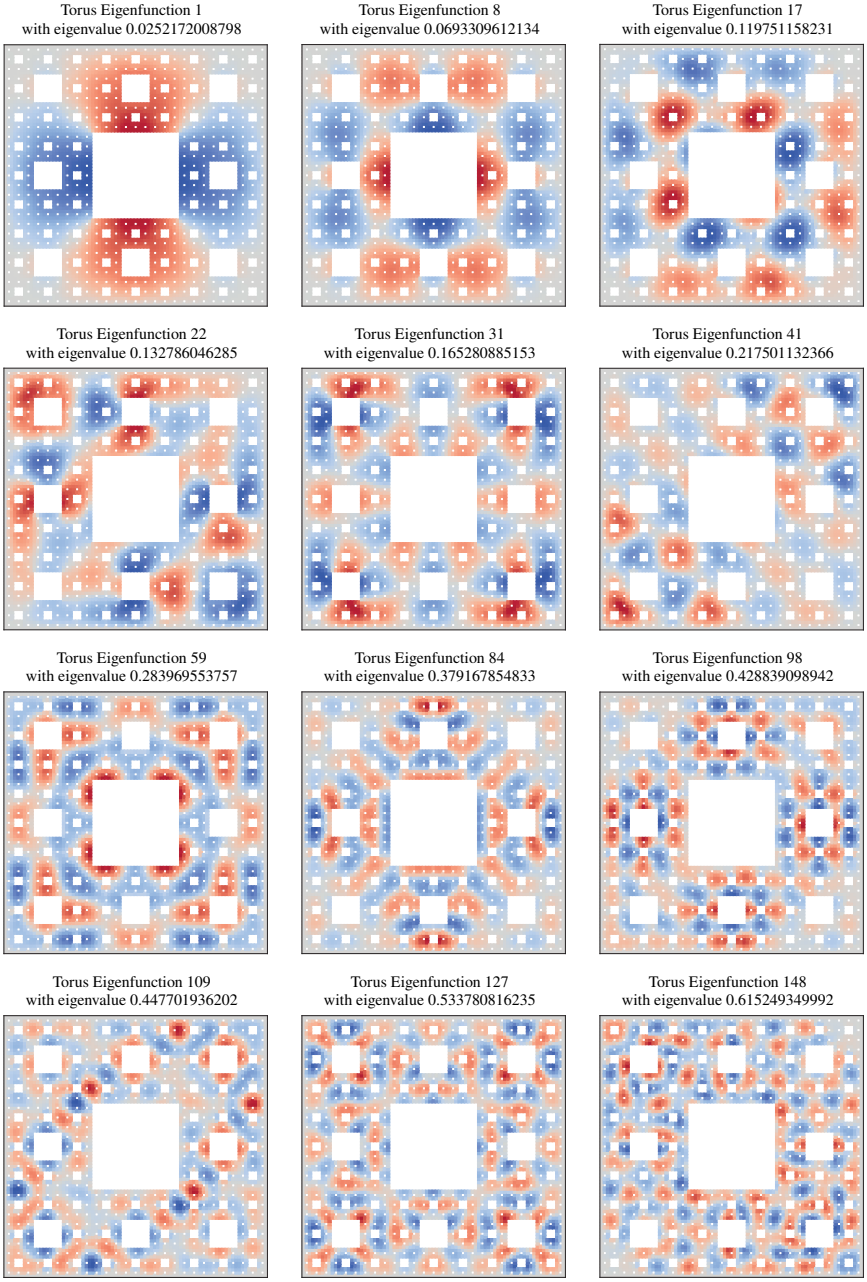

Figure 20. Some Dirichlet eigenfunctions with torus identifications.

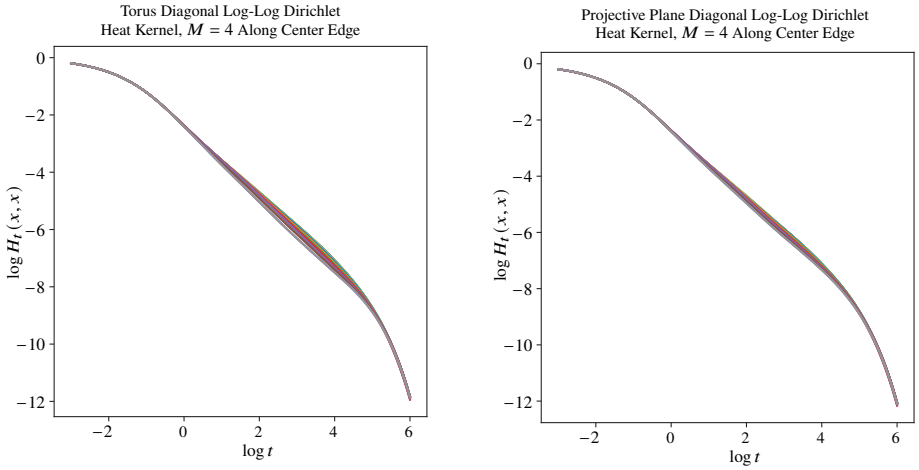

Figure 21. Log-log plot of the diagonal Dirichlet heat kernel for torus and projective identifications. (Klein identifications are similar.) Each plot is for a cell x bordering the interior square.

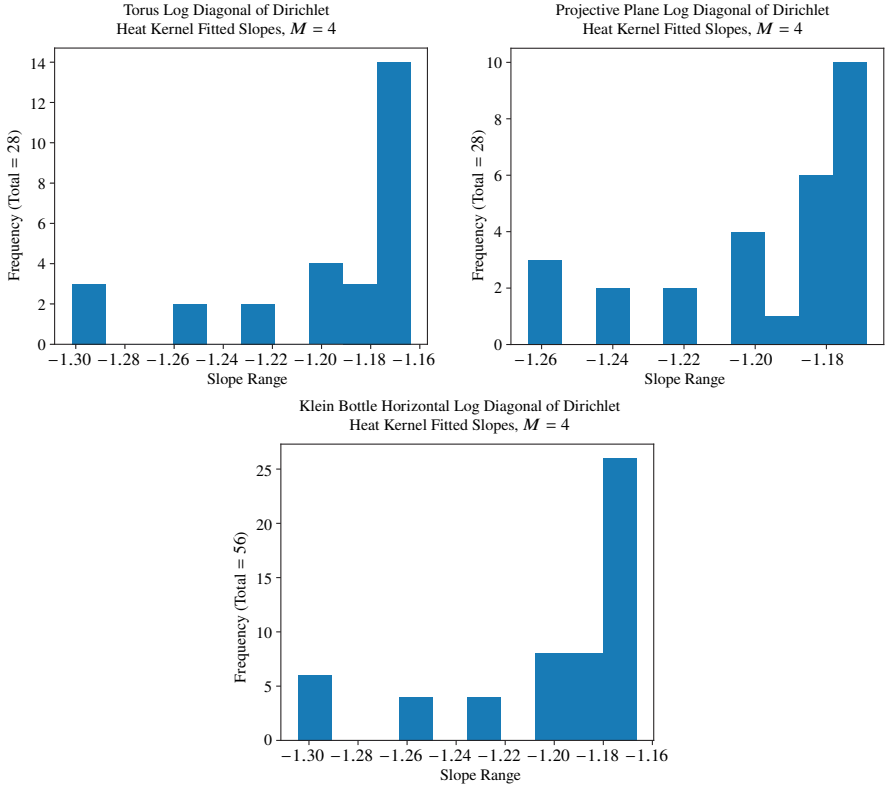

Figure 22. Histograms for slope values of Table 3.

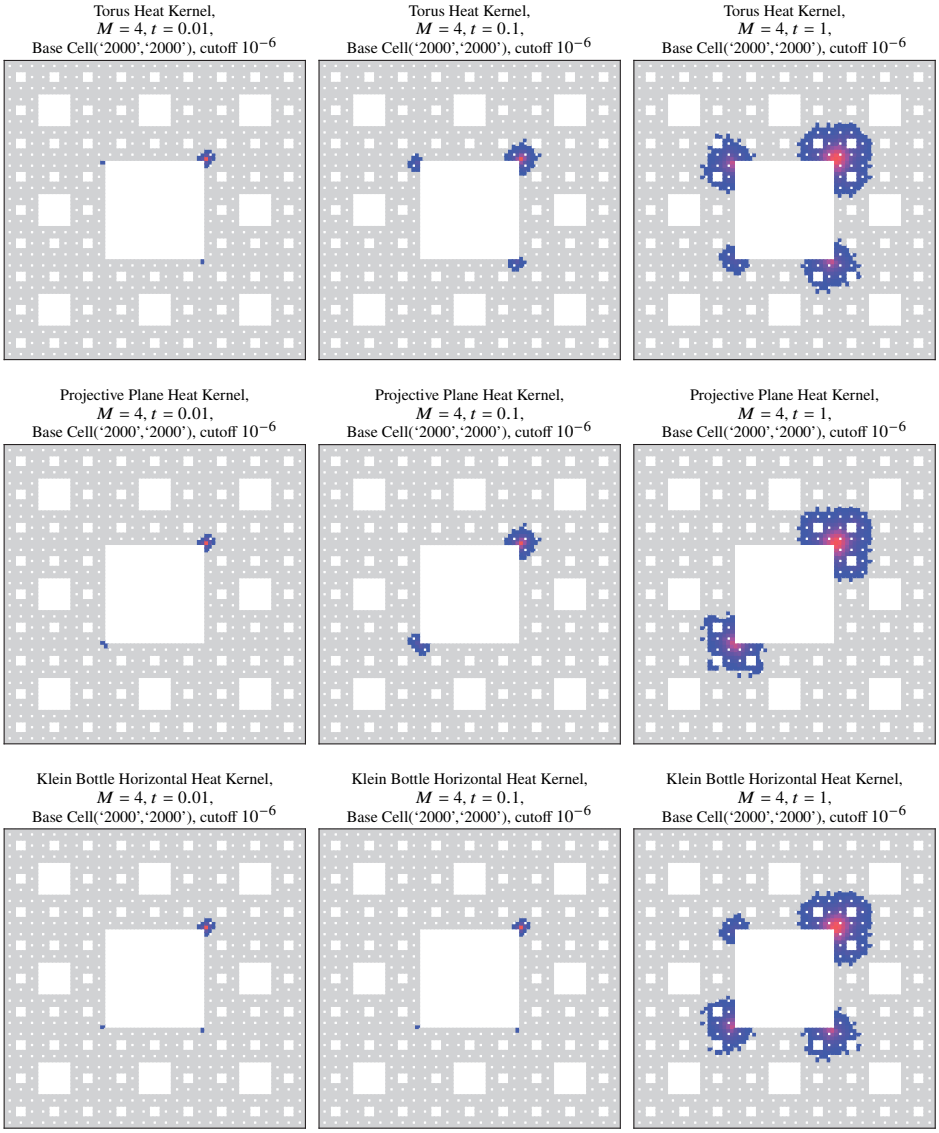

Figure 23. The off-diagonal heat kernel for torus (top), projective, and Klein horizontal (bottom) identifications at times $t = 0.01$ (left), 0.1, and 1 (right). Values with magnitude $< 10^{-6}$ are gray.

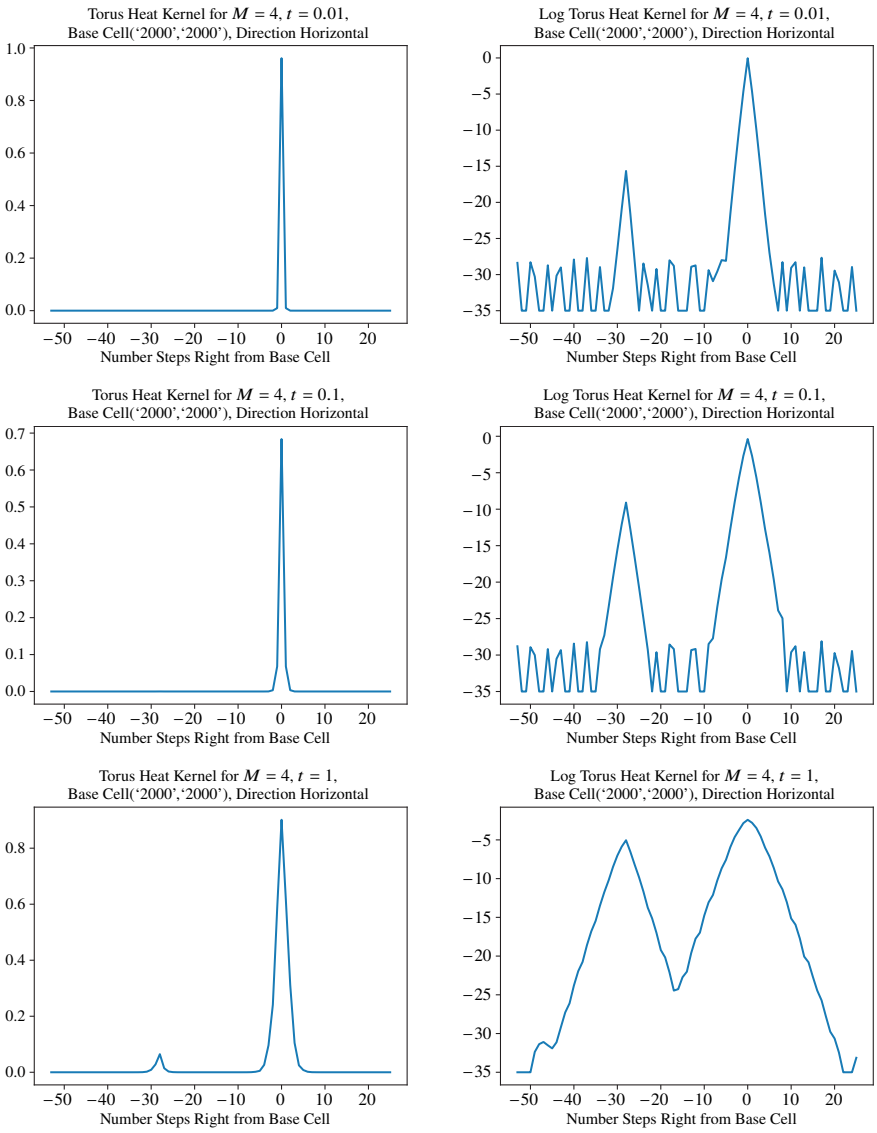

Figure 24. With torus identifications, the Dirichlet heat kernel along a horizontal line (left) and its log (right) at times $t = 0.01$ (top), 0.1, and 1 (bottom). Log values ≤ -30 are partly numerical error.

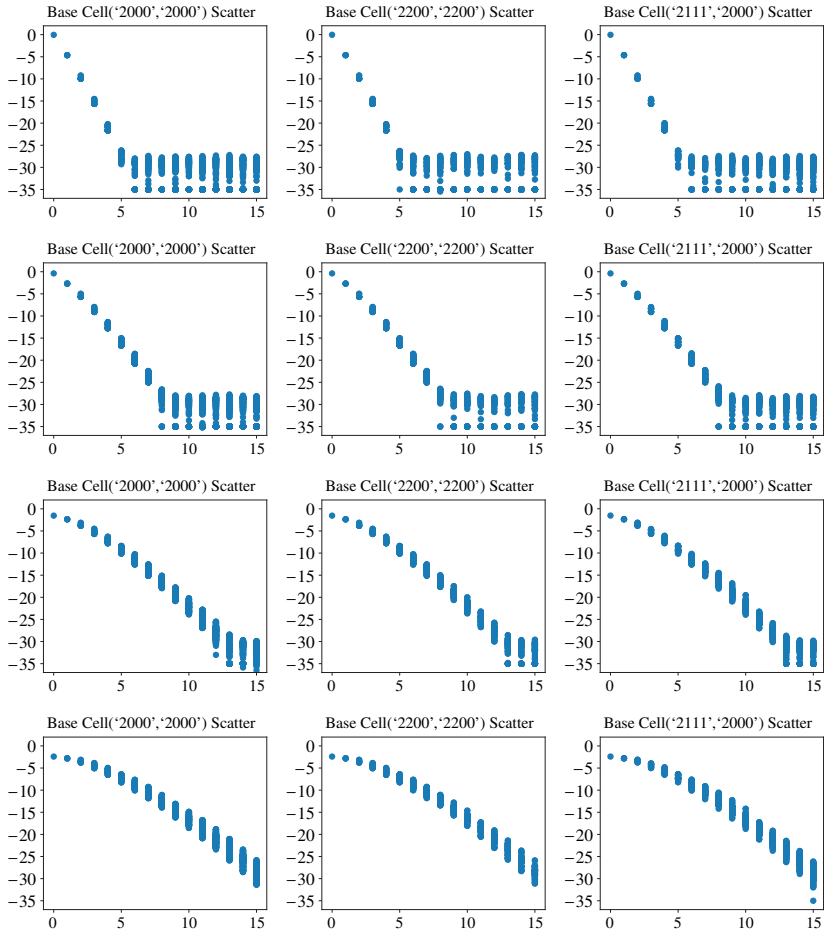

Figure 25. Log Dirichlet heat kernel plotted against distance to base cell, for three base cells (columns), times $t = 0.01$ (top), 0.1, 0.5, and 1 (bottom), and torus identifications. (Projective and Klein yield similar plots.)

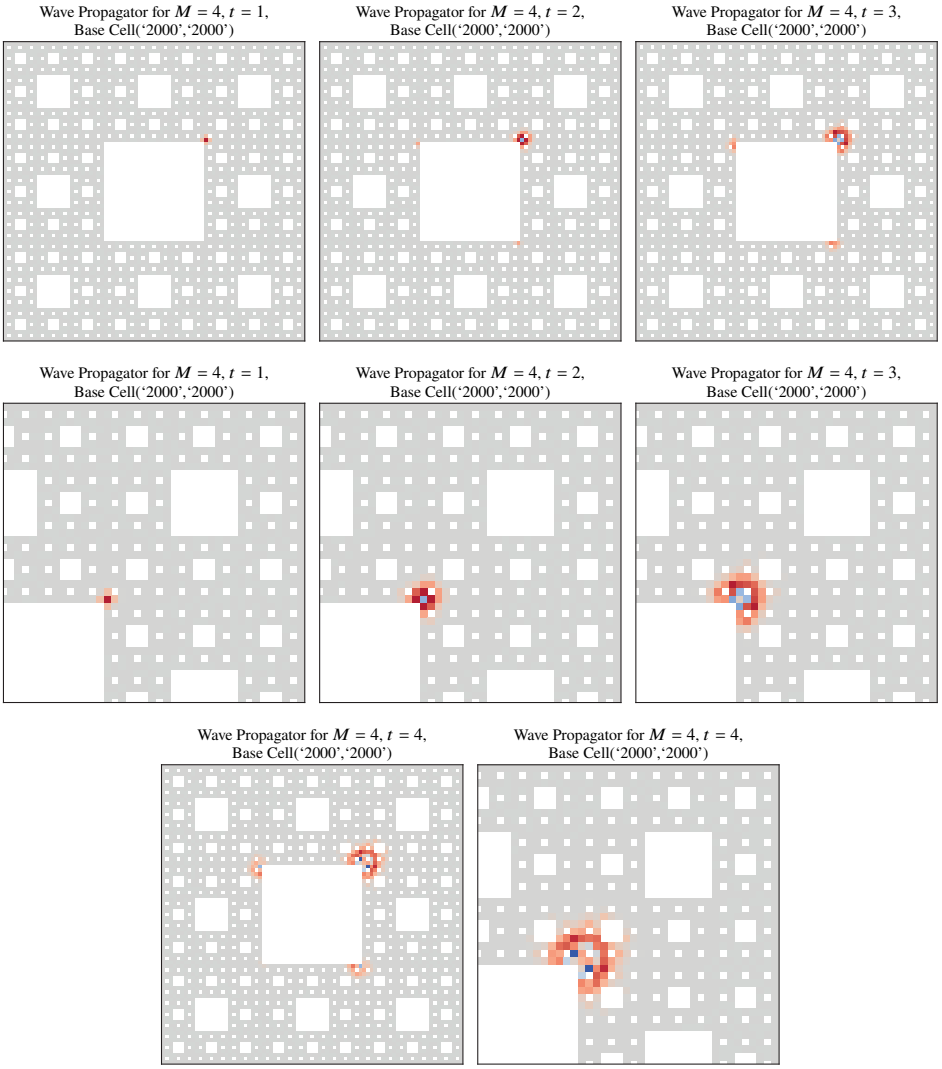

Figure 26. The wave propagator with torus identifications for one base cell is shown at times $t = 1, 2, 3$ (across the top) and $t = 4$ (bottom left). Below $t = 1, 2, 3$ and beside $t = 4$ are zoomed pictures showing some of the more prominent behavior.

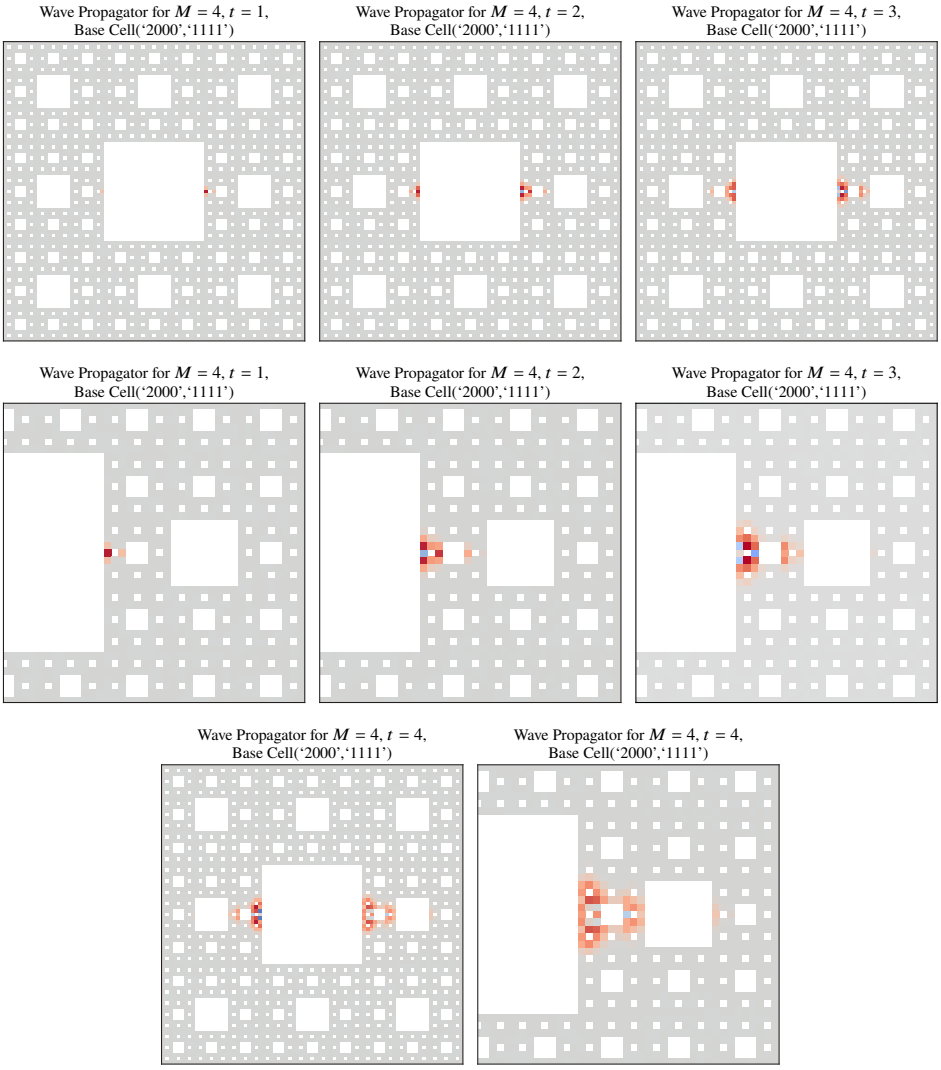

Figure 27. Refer to the description of Figure 26.

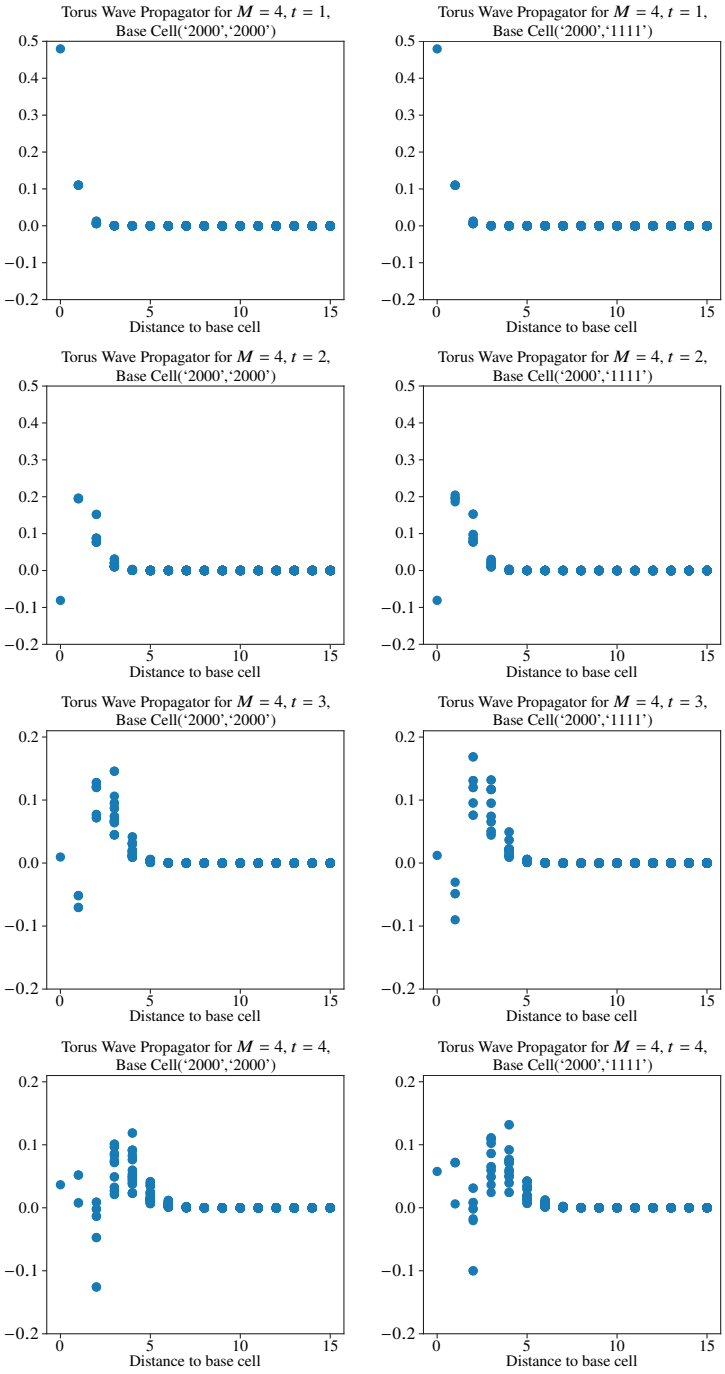

Figure 28. Scatter plots of the wave propagator. Columns (left to right) correspond to the base cells in Figures 26 and 27. Rows are times $t = 1, 2, 3, 4$.

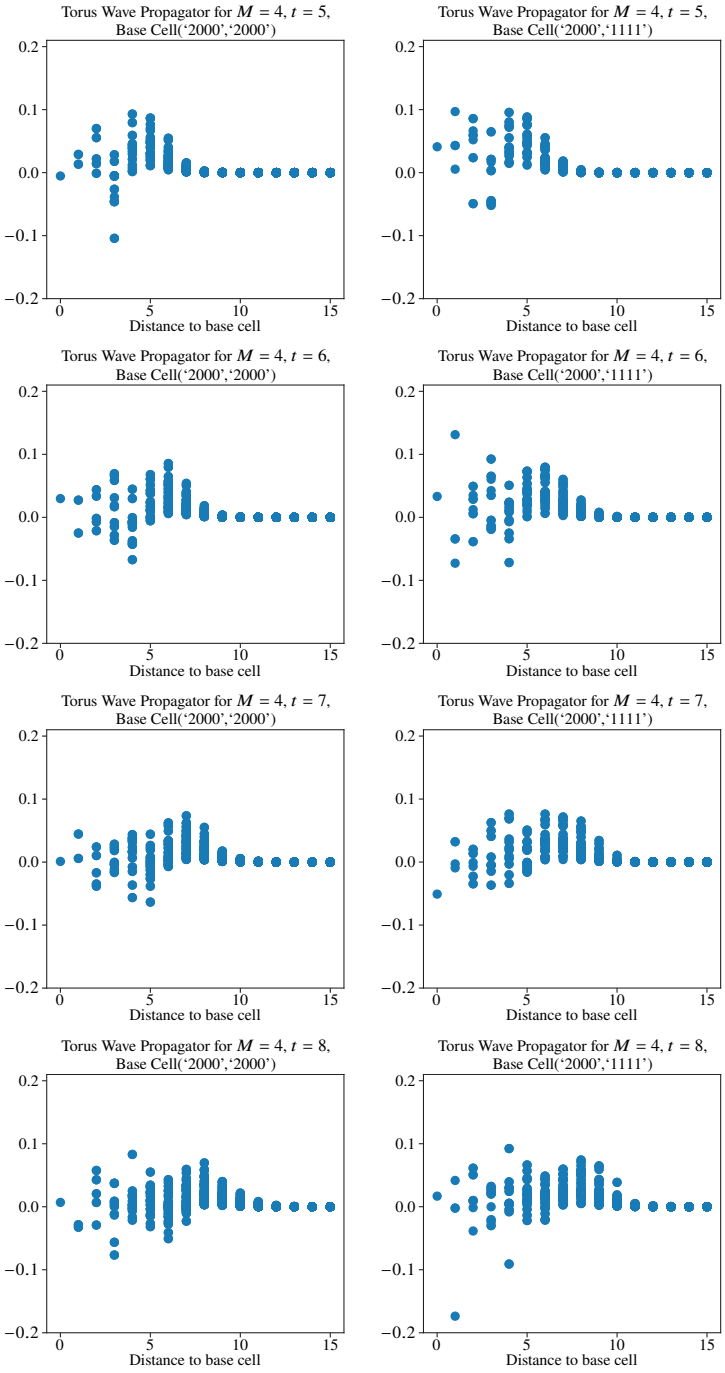

Figure 29. As in Figure 28, but with times $t = 5, 6, 7, 8$.

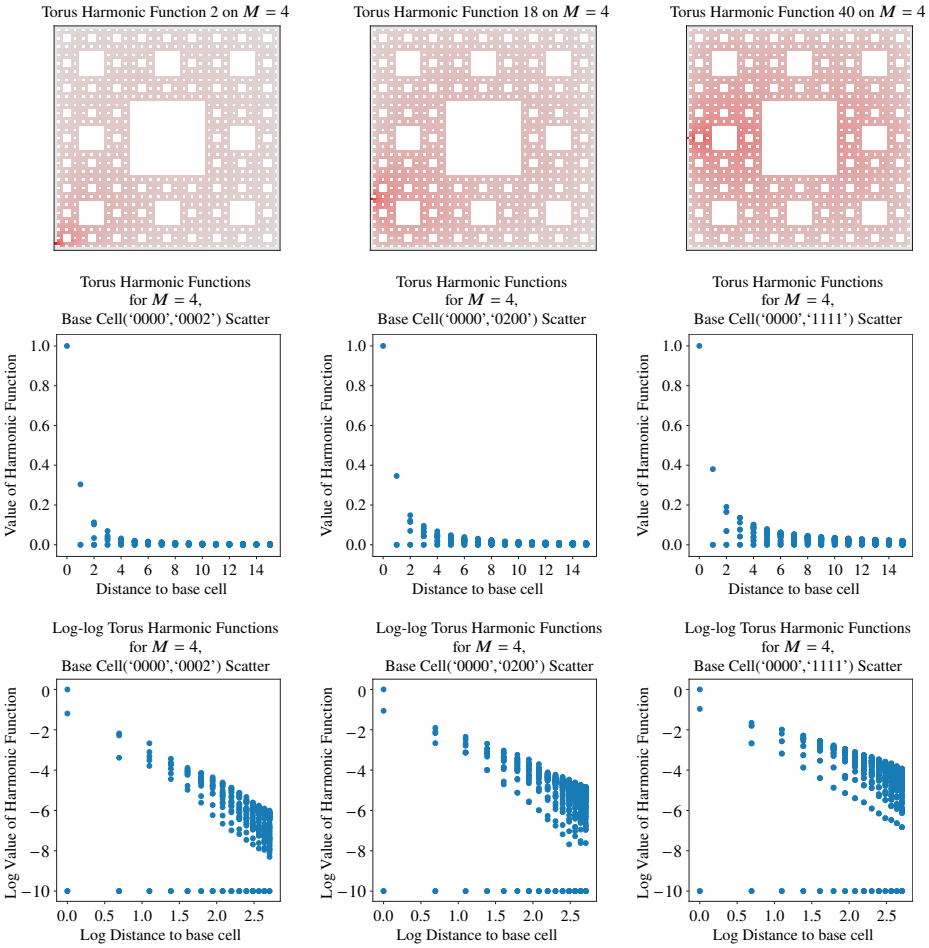

Figure 30. (Top Row) A sampling of $x \mapsto P(x, y)$ on $M = 4$, with y chosen to be three cells along the boundary. (Middle Row) For the same points y as above, the values of $x \mapsto P(x, y)$ plotted against $d(x, y) \leq 15$. (Bottom Row) Log-log versions of the plots shown in the middle row. Boundary cells are omitted in these plots.

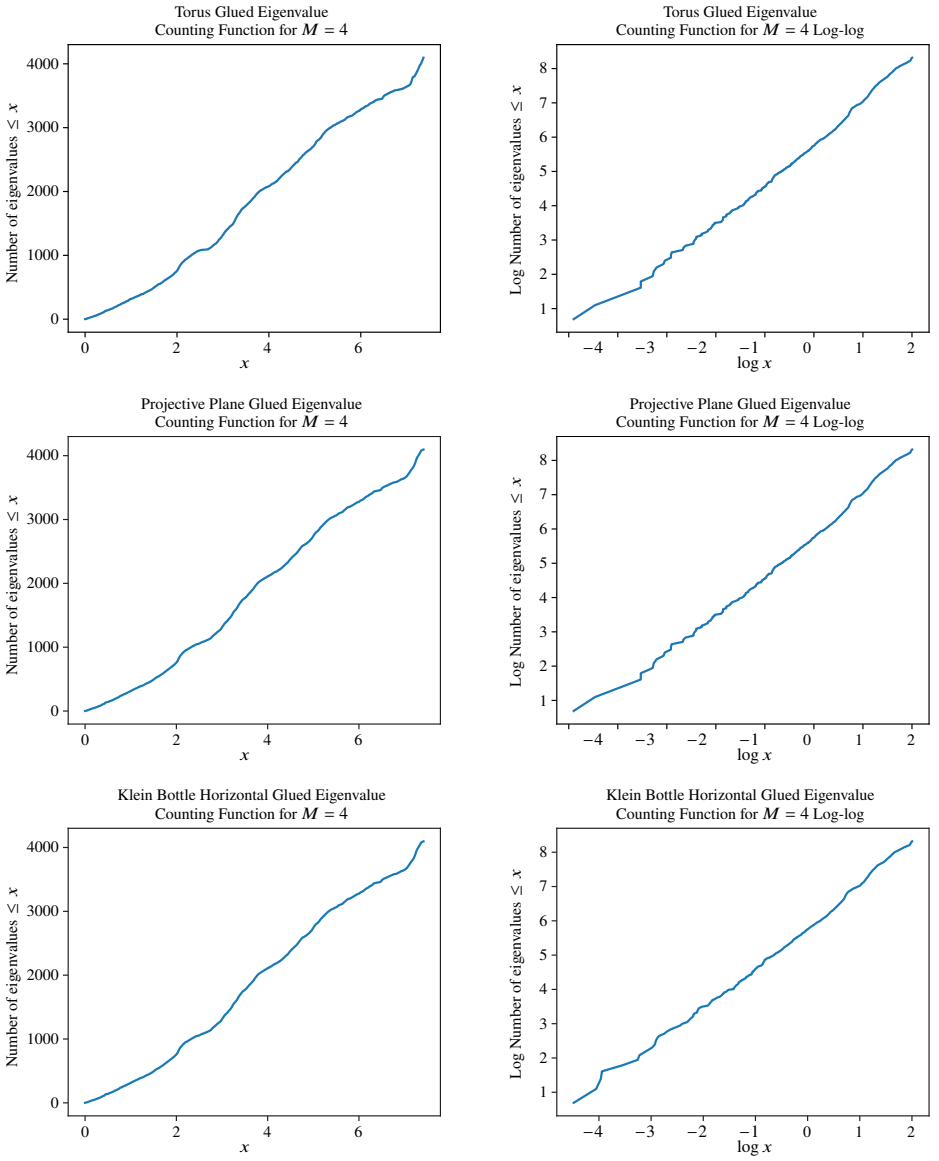

Figure 31. Eigenvalue counting functions (left) and their log-log counterparts (right).

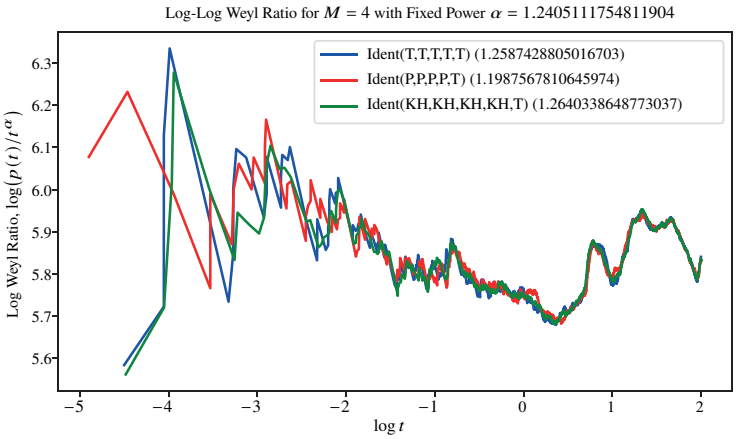

Figure 32. Weyl plots for torus (blue), projective (red), and Klein (green) identifications.

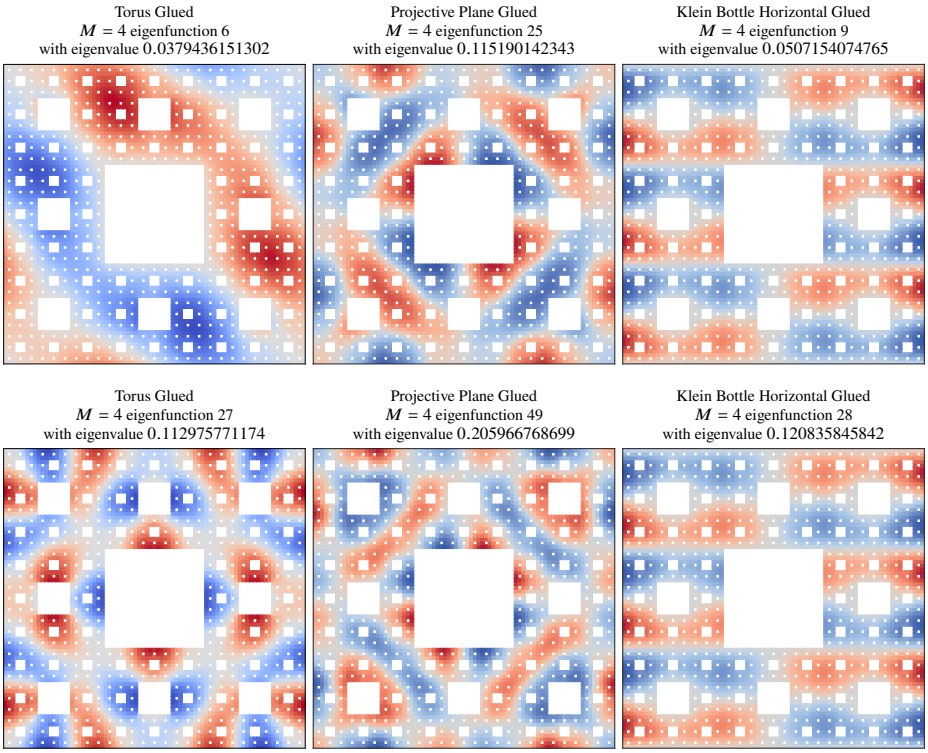

Figure 33. Sample torus glued (left), projective glued (middle), and Klein glued (right) eigenfunctions at level $m = 4$.

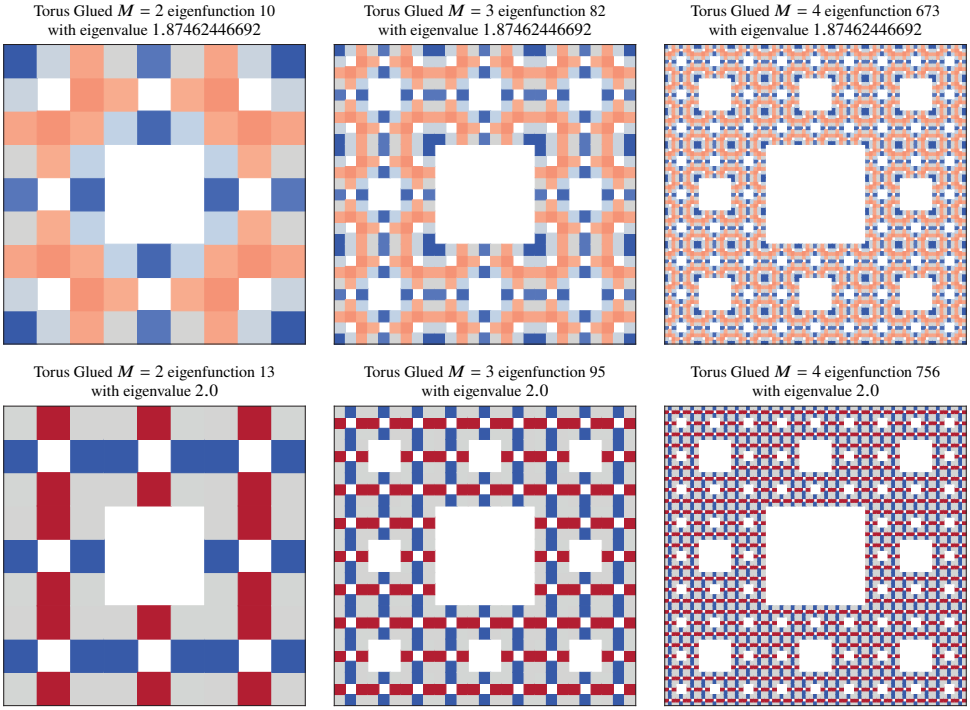

Figure 34. Two samples of miniaturization with torus glued identifications across levels $m = 2, 3, 4$.

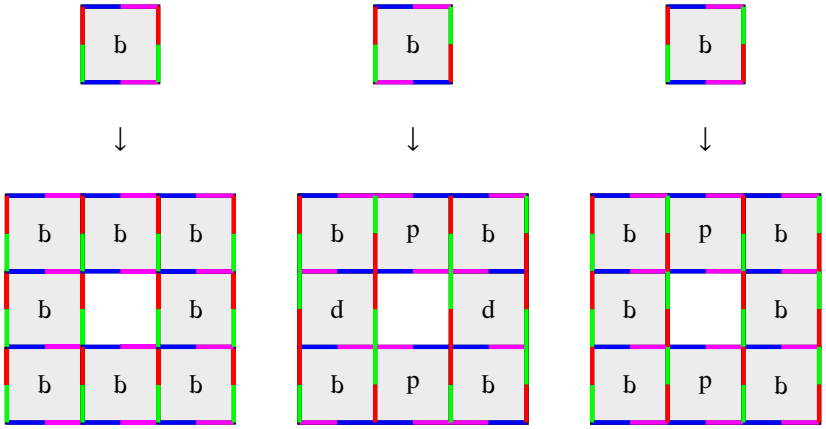

Figure 35. An eigenfunction on V_m is tiled to obtain an eigenfunction on V_{m+1}, either for torus (left), projective (middle), or Klein horizontal (right) identifications.

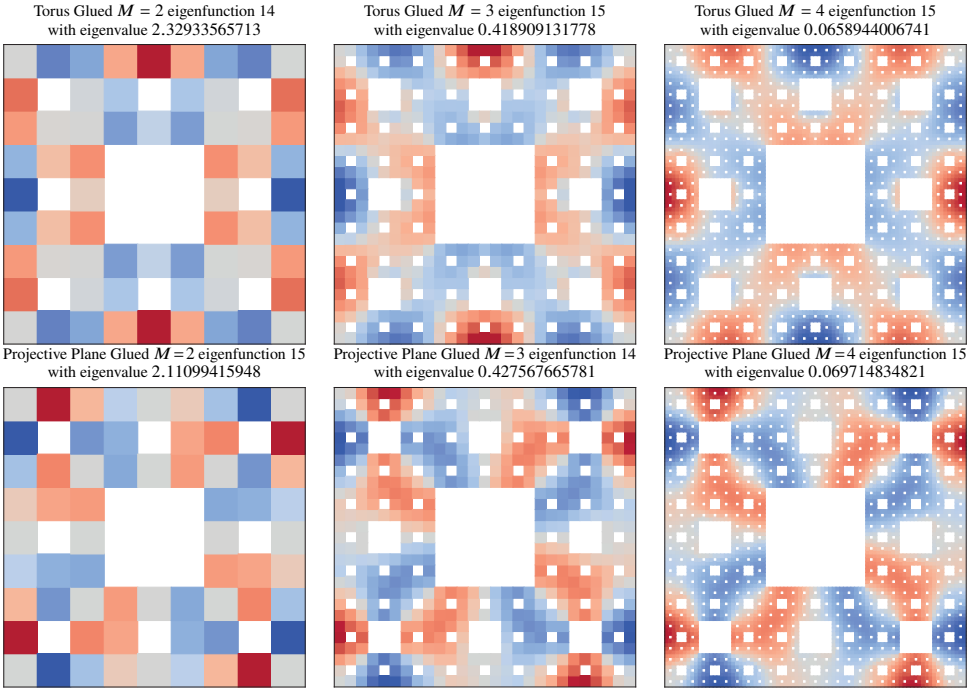

Figure 36. The top row shows an eigenfunction refining on *MCT* from level 2 (left) to levels 3 (middle) and 4 (right, negated). The bottom row is similar, but on *MCP*.

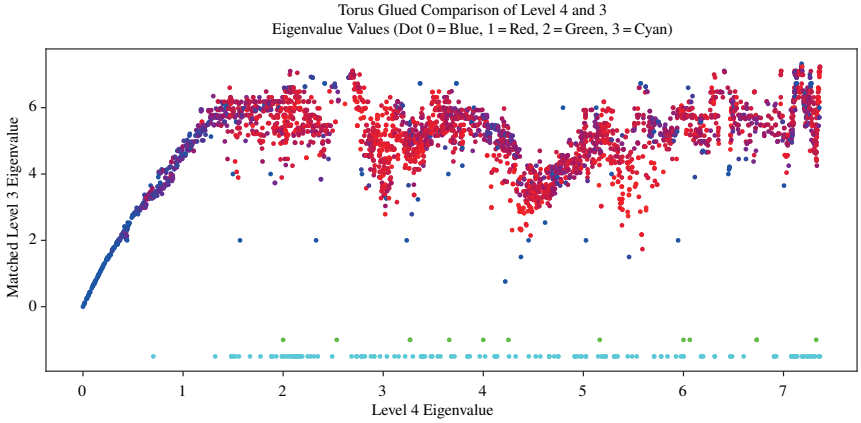

Figure 37. Matched eigenvalues from our refinement testing on levels $m = 3, 4$ with torus glued identifications. (Projective and Klein identifications yield similar plots.) Color indicates result quality: continuously from dark blue (refines well) to red (poor match); green ($\bar{u} = 0$); or cyan ($\text{proj}\,\bar{u} = 0$). Since green and cyan dots do not pair with level 3 eigenvalues, they are placed artificially along the bottom.

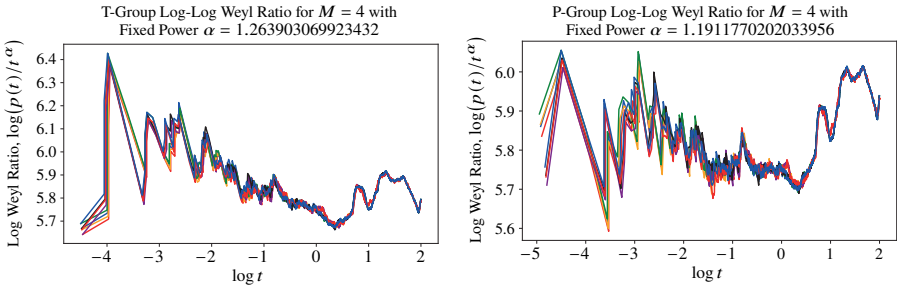

Figure 38. Weyl ratios for identifications beginning with torus (left) or projective (right) identifications.

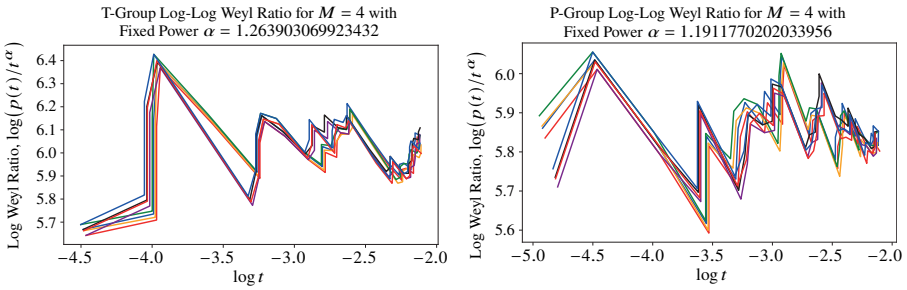

Figure 39. Zoomed version of Figure 38.

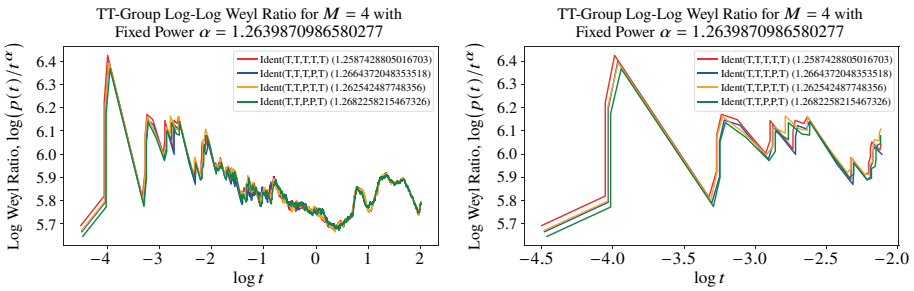

Figure 40. Weyl plots for identifications beginning $T, T, \ldots$ (left) and a zoom (right).

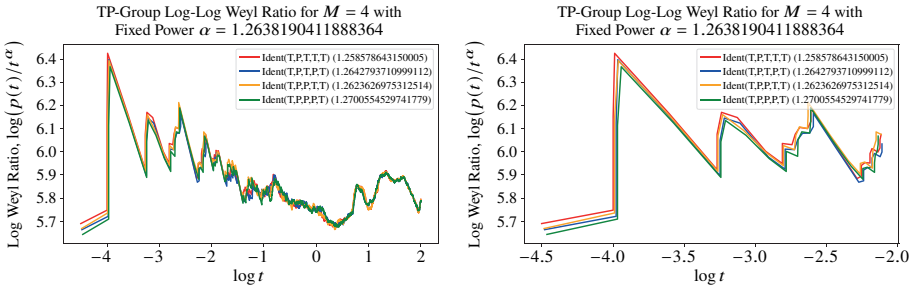

Figure 41. Weyl plots for identifications beginning $T, P, \ldots$ (left) and a zoom (right).

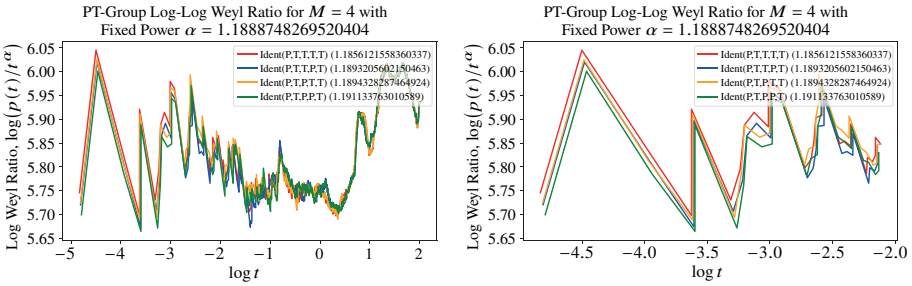

Figure 42. Weyl plots for identifications beginning $P, T, \ldots$ (left) and a zoom (right).

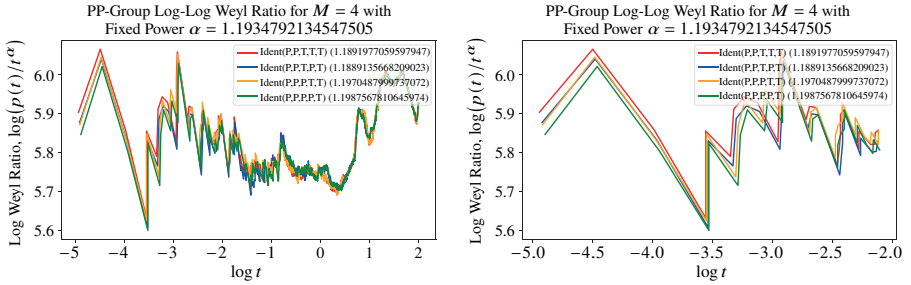

Figure 43. Weyl plots for identifications beginning $P, P, \ldots$ (left) and a zoom (right).

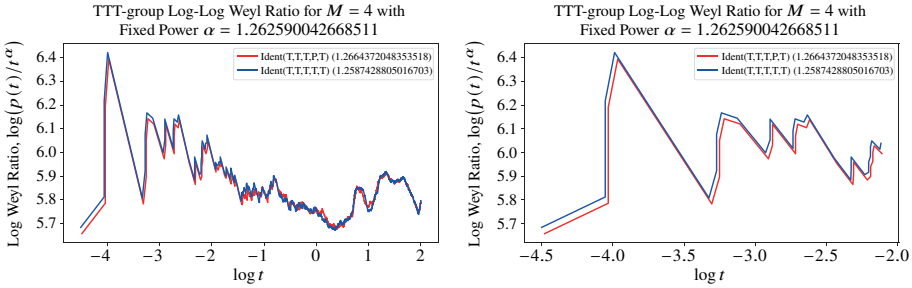

Figure 44. Weyl plots for identifications beginning $T, T, T, \ldots$ (left) and a zoom (right).

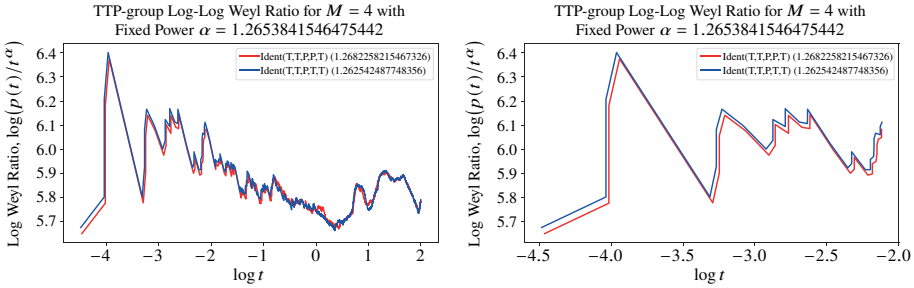

Figure 45. Weyl plots for identifications beginning $T, T, P, \ldots$ (left) and a zoom (right).

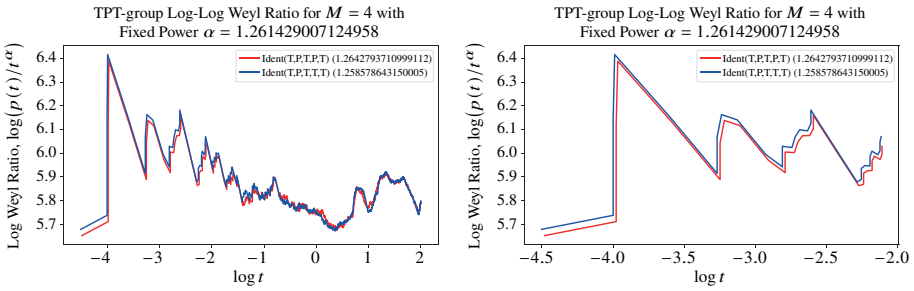

Figure 46. Weyl plots for identifications beginning $T, P, T, \ldots$ (left) and a zoom (right).

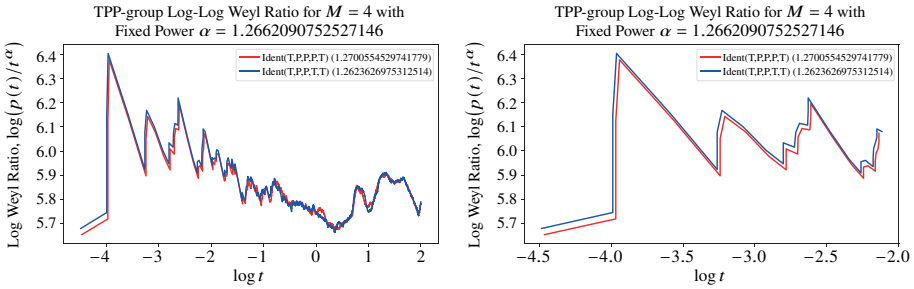

Figure 47. Weyl plots for identifications beginning $T, P, P \ldots$ (left) and a zoom (right).

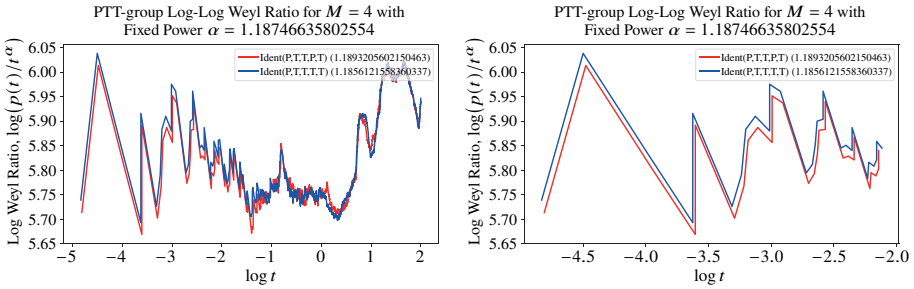

Figure 48. Weyl plots for identifications beginning $P, T, T, \ldots$ (left) and a zoom (right).

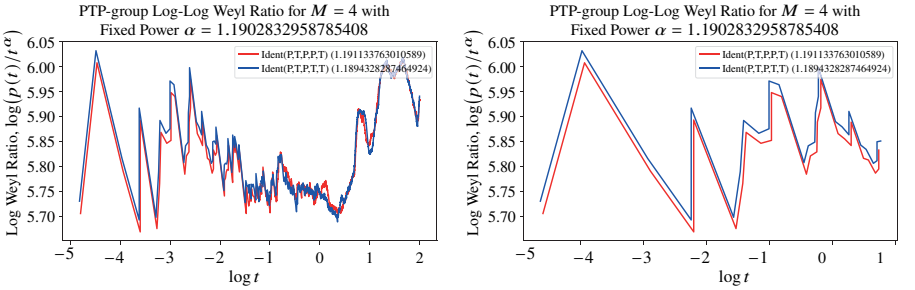

Figure 49. Weyl plots for identifications beginning $P, T, P, \ldots$ (left) and a zoom (right).

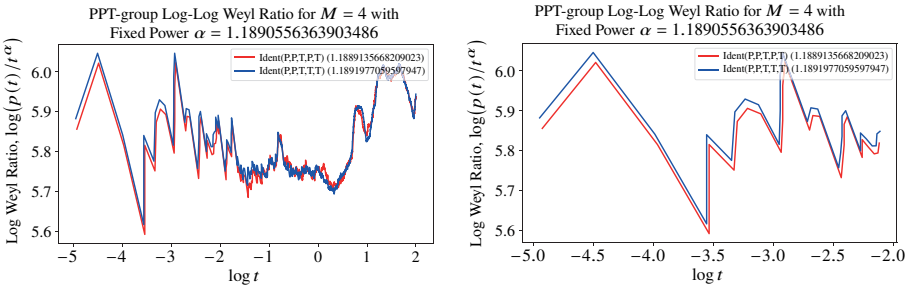

Figure 50. Weyl plots for identifications beginning $P, P, T, \ldots$ (left) and a zoom (right).

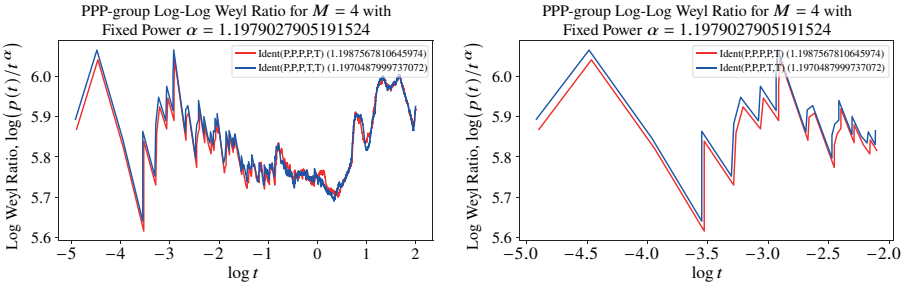

Figure 51. Weyl plots for identifications beginning $P, P, P, \ldots$ (left) and a zoom (right).

Acknowledgments.

We thank E. Goodman, who was supported by the Haverford College Koshland Integrated Natural Sciences Center and by a University of Pennsylvania Benjamin Franklin Fellowship, for doing simulations and numerical computations, for producing figures and plots and for insightful discussion on ball cardinality arguments and patterns of eigenvalues and eigenfunctions.

We thank the anonymous reviewers, whose valuable comments helped us improve the paper, included numerous references and possible future directions, and also guided us to the power-law approach in Section 3.

We are also deeply grateful to Alexander Teplyaev for their assistance in the publication process.

The numerical computations in this paper were done using the Python Programming Language [28], particularly with the packages NumPy [26, 32] and SciPy [33]. Many of the figures were generated with the Matplotlib package [20].

Funding. Chunyin Siu was supported by the Professor Charles K. Kao Research Exchange Scholarship 2015/16 and Croucher Scholarships for Doctoral Studies 2019/20.

References

[1] M. T. Barlow, Diffusions on fractals. In *Lectures on probability theory and statistics (Saint-Flour, 1995)*, pp. 1–121, Lecture Notes in Math. 1690, Springer, Berlin, 1998 Zbl 0916.60069 MR 1668115

[2] M. T. Barlow, Heat kernels and sets with fractal structure. In *Heat kernels and analysis on manifolds, graphs, and metric spaces (Paris, 2002)*, pp. 11–40, Contemp. Math. 338, Amer. Math. Soc., Providence, RI, 2003 Zbl 1056.60072 MR 2039950

[3] M. T. Barlow and R. F. Bass, The construction of Brownian motion on the Sierpiński carpet. *Ann. Inst. H. Poincaré Probab. Stat.* **25** (1989), no. 3, 225–257 Zbl 0691.60070 MR 1023950

[4] M. T. Barlow and R. F. Bass, Coupling and Harnack inequalities for Sierpiński carpets. *Bull. Amer. Math. Soc. (N.S.)* **29** (1993), no. 2, 208–212 Zbl 0782.60017 MR 1215306

[5] M. T. Barlow and R. F. Bass, Random walks on graphical Sierpinski carpets. In *Random walks and discrete potential theory (Cortona, 1997)*, pp. 26–55, Sympos. Math., XXXIX, Cambridge Univ. Press, Cambridge, 1999 Zbl 0958.60045 MR 1802425

[6] M. T. Barlow, R. F. Bass, and T. Kumagai, Stability of parabolic Harnack inequalities on metric measure spaces. *J. Math. Soc. Japan* **58** (2006), no. 2, 485–519 Zbl 1102.60064 MR 2228569

[7] M. T. Barlow, R. F. Bass, T. Kumagai, and A. Teplyaev, Uniqueness of Brownian motion on Sierpiński carpets. *J. Eur. Math. Soc. (JEMS)* **12** (2010), no. 3, 655–701 Zbl 1200.60070 MR 2639315

[8] M. T. Barlow, T. Coulhon, and T. Kumagai, Characterization of sub-Gaussian heat kernel estimates on strongly recurrent graphs. *Comm. Pure Appl. Math.* **58** (2005), no. 12, 1642–1677 Zbl 1083.60060 MR 2177164

[9] M. Begué, T. Kalloniatis, and R. S. Strichartz, Harmonic functions and the spectrum of the Laplacian on the Sierpinski carpet. *Fractals* **21** (2013), no. 1, 1350002, 32 MR 3042410

[10] M. Begue, D. J. Kelleher, A. Nelson, H. Panzo, R. Pellico, and A. Teplyaev, Random walks on barycentric subdivisions and the Strichartz hexacarpet. *Exp. Math.* **21** (2012), no. 4, 402–417 Zbl 1263.28002 MR 3004256

[11] J. Bello, Y. Li, and R. S. Strichartz, Hodge–de Rham theory of K-forms on carpet type fractals. In *Excursions in harmonic analysis. Vol. 3*, pp. 23–62, Appl. Numer. Harmon. Anal., Birkhäuser/Springer, Cham, 2015 Zbl 1323.28008 MR 3380405

[12] P. G. Doyle and J. L. Snell, *Random walks and electric networks*. Carus Mathematical Monographs 22, Mathematical Association of America, Washington, DC, 1984 Zbl 0583.60065 MR 920811

[13] S. Drenning and R. S. Strichartz, Spectral decimation on Hambly's homogeneous hierarchical gaskets. *Illinois J. Math.* **53** (2009), no. 3, 915–937 (2010) Zbl 1211.28005 MR 2727362

[14] M. Fukushima and T. Shima, On a spectral analysis for the Sierpiński gasket. *Potential Anal.* **1** (1992), no. 1, 1–35 Zbl 1081.31501 MR 1245223

[15] E. Goodman, C. Siu, and R. S. Strichartz, Research website. Available at: http://www.math.cornell.edu/~etg35/. Acquired Jan 2, 2017

[16] B. M. Hambly, Brownian motion on a homogeneous random fractal. *Probab. Theory Related Fields* **94** (1992), no. 1, 1–38 Zbl 0767.60075 MR 1189083

[17] B. M. Hambly, Brownian motion on a random recursive Sierpinski gasket. *Ann. Probab.* **25** (1997), no. 3, 1059–1102 Zbl 0895.60081 MR 1457612

[18] B. M. Hambly, Heat kernels and spectral asymptotics for some random Sierpinski gaskets. In *Fractal geometry and stochastics, II (Greifswald/Koserow, 1998)*, pp. 239–267, Progr. Probab. 46, Birkhäuser, Basel, 2000 Zbl 0947.60086 MR 1786351

[19] D. J. Kelleher, H. Panzo, A. Brzoska, and A. Teplyaev, Dual graphs and modified Barlow-Bass resistance estimates for repeated barycentric subdivisions. *Discrete Contin. Dyn. Syst. Ser. S* **12** (2019), no. 1, 27–42 Zbl 1411.60115 MR 3836590

[20] J. D. Hunter, Matplotlib: A 2D graphics environment. *Computing in Science & Engineering* **9** (2007), no. 3, 90–95

[21] J. Kigami, *Analysis on fractals*. Cambridge Tracts in Mathematics 143, Cambridge University Press, Cambridge, 2001 Zbl 0998.28004 MR 1840042

[22] S. Kusuoka and Z. X. Yin, Dirichlet forms on fractals: Poincaré constant and resistance. *Probab. Theory Related Fields* **93** (1992), no. 2, 169–196 Zbl 0767.60076 MR 1176724

[23] Y. T. Lee, Infinite propagation speed for wave solutions on some post-critically finite fractals. In *Analysis, probability and mathematical physics on fractals*, pp. 503–519, Fractals Dyn. Math. Sci. Arts Theory Appl. 5, World Sci. Publ., Hackensack, NJ, [2020] ©2020 Zbl 1454.35230 MR 4472260

[24] D. Lenz and A. Teplyaev, Expansion in generalized eigenfunctions for Laplacians on graphs and metric measure spaces. *Trans. Amer. Math. Soc.* **368** (2016), no. 7, 4933–4956 Zbl 1332.81069 MR 3456166

[25] D. Molitor, N. Ott, and R. Strichartz, Using Peano curves to construct Laplacians on fractals. *Fractals* **23** (2015), no. 4, 1550048, 29 Zbl 1342.28020 MR 3433413

[26] T. E. Oliphant, *A guide to NumPy*. 1, Trelgol Publishing USA, 2006

[27] T. Poerschke, G. Stolz, and J. Weidmann, Expansions in generalized eigenfunctions of selfadjoint operators. *Math. Z.* **202** (1989), no. 3, 397–408 Zbl 0661.47021 MR 1017580

[28] Python Software Foundation, Python Language Reference, Python 2.7.

[29] M. Reed and B. Simon, *Methods of modern mathematical physics. IV. Analysis of operators*. Academic Press [Harcourt Brace Jovanovich, Publishers], New York–London, 1978 MR 0493421

[30] R. S. Strichartz, *Differential equations on fractals*. Princeton University Press, Princeton, NJ, 2006 Zbl 1190.35001 MR 2246975

[31] R. S. Strichartz and A. Teplyaev, Spectral analysis on infinite Sierpiński fractafolds. *J. Anal. Math.* **116** (2012), 255–297 Zbl 1272.28012 MR 2892621

[32] S. Van Der Walt, S. C. Colbert, and G. Varoquaux, The NumPy array: a structure for efficient numerical computation. *Computing in Science & Engineering* **13** (2011), no. 2, 22–30

[33] P. Virtanen, R. Gommers, T. E. Oliphant et al. SciPy 1.0: Fundamental Algorithms for Scientific Computing in Python. *Nat. Methods* **17** (2020), 261–272

[34] W. Woess, *Random walks on infinite graphs and groups*. Cambridge Tracts in Mathematics 138, Cambridge University Press, Cambridge, 2000 Zbl 0951.60002 MR 1743100

Chunyin Siu
Center for Applied Mathematics, Cornell University, 657 Frank H.T. Rhodes Hall, Cornell University, Ithaca, NY 14853, USA; cs2323@cornell.edu

Robert S. Strichartz
Robert S. Strichartz passed away on 19 December 2021. His affiliation was Cornell University, Ithaca, USA.